Cluster Model studies of Nuclei in the Actinide Region

H.E. Seals
Department of Physics, University of Cape Town

March 11, 2006

Thesis submitted in fulfillment of the requirements for the degree of Master of Science at the University of Cape Town.

Abstract

Three independent techniques for obtaining core-cluster partitions of nuclei in the actinide region are found to give consistent results. As a by-product the techniques generate theoretical decay constants and energy spectra in good agreement with their experimental counterparts. The relationship implied by the binary cluster model between core-cluster charge products and electric quadrupole transition strengths is confirmed; and a basis from which to extract quantitative information from Casten's correlations is introduced.

Contents

Acknowledgements

Many thanks firstly to my supervisor Prof S.M. Perez, who went far beyond the call of duty. To the National Research Foundation and University of Cape Town (specifically the Harry Crossley, K.W. Johnstone and Joseph Stone funds) for their generous financial support. And finally my friends and family for all the love and prayers. (Eccl 12:12-14)

Chapter 1

Introduction: Nuclear Models

The unexpected alpha back scattering observed by Geiger and Marsden in 1911 led Rutherford to postulate his model of the nucleus. This was instrumental in the development of the Bohr model of the atom in which most of the atom's mass is concentrated in a very small positively charged nucleus at its centre. Rutherford's continued work in alpha scattering led to the transmutation of atoms, and isolation of the proton as a fundamental particle [1]. Chadwick's discovery of the neutron in 1931 completed the basic picture of the nucleus we have today in which the nucleons (protons and neutrons) are the basic constituents. More recently the internal structure of the nucleon has been probed revealing its three quark nature. However, above the level of quarks and gluons, there is still uncertainty around the arrangement and interaction of nucleons inside the nucleus. Despite the large body of knowledge about the nucleus, most models rely on empirically determined parameters and questions still abound.

Various models of the nucleus have been proposed, most of which explain only some aspects of nuclear behaviour. This thesis will examine the cluster model, weigh it up against some of the more established models and test it against data on three different properties of the nucleus; namely, the exotic decays, the spectra, and the quadrupole transition strengths of nuclei in the trans-Pb region. These various aspects will be explored in Chapters 3, 5 and 6 respectively. A detailed description of the cluster model is given in Chapter 2. Leading up to this, the shell model and collective models will be discussed in the remainder of this chapter, together with a brief introduction to the cluster model.

1.1 The Shell Model

Unlike the electromagnetic force that governs the structure of the atom, the nuclear force is very strong, with interaction energies of the order of MeV, and very short range, of the order of fm. Nucleons principally feel the effect of those nucleons nearest them and the force saturates. Thus the binding energy per nucleon and the central nucleon density are almost independent of the number of nucleons within the nucleus.

The independent particle model is based on two main premises, first that the nu-

cleons move independently in an average potential; and second that the energy levels are filled from the lowest energy to the highest, in accordance with the Pauli exclusion principle which prohibits two identical particles from occupying the same state [2]. Since all the low energy states are filled any residual scattering involves high energy final states and is thus reduced. So the nucleons can be said to move largely independently of one another, despite the strong short range force.

With such an average potential, the nucleus resembles the atom where electrons are ordered in shells. Discontinuities occur at shell closures designating the magic numbers. The existence of actual magic numbers provided strong motivation to investigate the independent particle model of the nucleus. When the proton or neutron number is one of these numbers {2, 8, 20, 28, 50, 82, 126} distinctive properties appear. These magic nuclei are more stable than their neighbours, and their first excited state occurs at a higher excitation energy. The natural abundances of these magic nuclei are noticeably larger, they appear regularly as decay products, and their neutron absorption cross section is uncommonly small. Also, following from the inert nature of the closed shell, the behaviour of nuclei either side of a shell closure is dominated by the extra or missing nucleon. When there is more than one valence nucleon the interaction between them is no longer negligible as, outside the closed shell, there are unoccupied low energy states. So, to describe the system, an appropriate superposition of all the independent particle states is required. The resulting shell model wavefunction for a many valence nucleon system is thus extremely complex.

An average potential needs to be chosen such that the magic numbers are reproduced correctly. The square well is a simple choice for such a potential, for which

$$V_0(\vec{r}) = \begin{cases} -V_0 & r \leq R \\ 0 & r > R \end{cases} \tag{1.1}$$

with V_0 of the order of MeV and $R \approx r_0 A^{1/3}$, with A the mass number and the nuclear radius parameter $r_0 \approx 1.2$ fm. Another simple analytical potential is the harmonic oscillator, defined by

$$V_0(\vec{r}) = \frac{1}{2} m\omega^2 r^2. \tag{1.2}$$

The above, and other similar potentials, fail to reproduce the magic numbers. This can be achieved by coupling the spin $\vec{s}$ to the orbital angular momentum $\vec{l}$ through a spin-orbit interaction. The Schrodinger equation becomes

$$\hat{H}\Psi = \left[-\frac{\hbar^2}{2m}\nabla^2 + V_0(r) + V_{s.o.}(r)\vec{l}\cdot\vec{s} \right] \Psi = E\Psi \tag{1.3}$$

with each independent particle state an eigenfunction of $\hat{H}$. The spin-orbit interaction splits the $2(2l+1)$ degeneracy of each level into two levels of degeneracy $(2j_+ + 1)$ and $(2j_- + 1)$ where the total angular momentum is $\vec{j} = \vec{l} + \vec{s}$ and $j_\pm = l \pm 1/2$. All the magic numbers can then be reproduced.

A widely accepted nuclear potential is the Saxon Woods potential, whose form mimics the nuclear density. Batty and Greenlees [3] used it to successfully reproduce the properties of closed shell ± 1 nucleon nuclei, and obtained charge distributions for closed shell nuclei that gave good fits to electron scattering data. The general form of the potential they used is

$$V(r) = V_C(r) - V_0 f(x_0) - V_{s.o.} \left(\frac{\hbar}{m_\pi c}\right)^2 \frac{1}{r}\frac{d}{dr} f(x_{s.o.}) \vec{l} \cdot \vec{s} \tag{1.4}$$

where $V_C(r)$ is the Coulomb potential due to a uniform charged sphere, and

$$f(x_n) = \frac{1}{1 + \exp\left\{\frac{(r-R_n)}{a_n}\right\}}. \tag{1.5}$$

In Eq. (1.4) $V_0 \approx 50$ MeV, $V_{s.o} \approx 5$ MeV, and different values of the parameters a_n and $R_n = r_n A^{1/3}$ are used, with $a_n \approx 0.70$ fm and $r_n \approx 1.20$ fm.

The interactions between valence nucleons can be taken into account by the expanding the nuclear wavefunction in terms of a set of independent particle wavefunctions. When there are many valence nucleons a large number of independent particle configurations must be included and a correspondingly large Hamiltonian matrix has to be diagonalised. This is computationally cumbersome and the resulting many component nuclear wavefunctions become difficult to interpret physically.

1.2 The Vibrational and Rotational Models

The shell model starts from the premise of independent nucleon motion. The enhancement of quadrupole transition strengths observed as the number of extra-core nucleons increases [4], suggests however that a substantial amount of charge is involved in these transitions. Although such collective behaviour can be mimicked by extensive shell model calculations, it is worthwhile to examine models in which collective behaviour is inherent. In this and the next section three such models, including the cluster model, will be discussed.

A generation after the basic theory of the atom had been successfully outlined by Niels Bohr, his son Aage and Ben Mottelson compiled a comprehensive study of collective nuclear motion by introducing the vibrational and the rotational models.

1.2.1 The Vibrational Model

The vibrational model proposes nuclear oscillations about a spherical shape. Lord Rayleigh's work on the classical liquid drop is a useful basis from which to start. Using normal coordinates $\alpha_{l\lambda}$ vibrations can be formulated by the expression

$$\mathrm{R}(t, \theta, \phi) = \mathrm{R}_0 \left[1 + \sum_{l\lambda} \alpha_{l\lambda}(t) Y_{l\lambda}(\theta, \phi)\right], \tag{1.6}$$

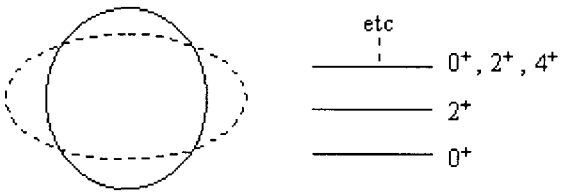

Figure 1.1: *Spectra generated by the vibrational model.*

where $R(t, \theta, \phi)$ describes the surface of the nuclear volume [5]. Modes with $l = 0$ and $l = 1$ are forbidden. The case with $l = 0$, known as the breathing mode, corresponds to a radial dependence on time only. The nucleus expands and contracts with a certain frequency. As nuclear matter is highly incompressible, such a vibrational mode requires a high excitation energy, and no low-lying breathing mode is expected. For $l = 1$ "the deformation gives a translation without change in shape" [5] and is unphysical in a system without any external forces acting upon it. The spectra resulting from the vibrational modes $l \geq 2$ are equally spaced with separation

$$\Delta E_l = \hbar \sqrt{\frac{C_l}{B_l}} \tag{1.7}$$

where B_l and C_l are the inertial and spring constants, respectively. ΔE_l increases with the multipolarity, l. The lowest states of the characteristic spectrum corresponding to zero, one, two,... quadrupole phonons are shown in Figure 1.1. The vibrational model is reasonably successful in describing near magic nuclei such as the Te isotopes [6].

1.2.2 The Rotational Model

Further from a closed shell the nuclear shape is assumed to be permanently distorted. A rotation of such a deformed nucleus can be described in terms of the system's three Euler angles, that relate the space- and body-fixed coordinate systems. The rotational degrees of freedom are limited by the various symmetries imposed on the deformed nucleus. For an even-even nucleus, axial symmetry about a body-fixed axis, together with reflectional invariance in the plane perpendicular to that axis of symmetry, yields a ground state band (K=0) of $J^\pi = 0^+, 2^+, 4^+, \ldots$ states as shown in Figure 1.2 with energies

$$E_J = \frac{\hbar^2}{2I} J\,(J+1) \tag{1.8}$$

where I is the moment of inertia.

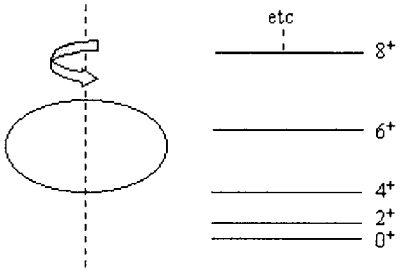

Figure 1.2: *Spectra generated by the rotational model.*

1.3 The Cluster Model

The cluster model incorporates many of the elements of the above models. Like the shell model it differentiates between the nucleons within a closed shell and the valence nucleons. By lumping all the valence nucleons together into a cluster it avoids the difficulties inherent in taking account of their mutual interactions. This is conceptually pleasing especially in cases when the subsystems of nucleons are particularly stable, for instance ^{20}Ne modelled as $^{16}\mathrm{O} + \alpha$ [7].

Wildermuth et al. introduced the cluster model in 1958 describing the clustering phenomena as an "energetically favoured correlation between nucleons" [8]. They describe in detail the case of ^{8}Be, modelled as two alpha clusters. An even-even nucleus comprised of a spinless even-even core and cluster is typical of the applications of the cluster model considered in this thesis. For such energetically favoured internal states, the core and cluster resist excitation, and any additional energy appears in their relative motion. The band of states produced are characterised by a single global quantum number $G = 2n + L$, where n is the number of nodes and L is the orbital angular momentum of a state. This will be discussed further in Chapter 2. For an even value of G the characteristic ground state band of an even-even nucleus with $J^\pi = L^\pi = 0^+, 2^+, 4^+ \ldots$ emerges without additional symmetry postulates.

As with the vibrational and rotational models, the cluster model is intrinsically collective since all the nucleons in the core and cluster follow the motion of their respective centres of mass. There is notable diversity in the spectra produced by the cluster model. For a larger cluster, in the mid-shell region, the spectrum is rotational-like as in the case of $^{232}\mathrm{U} \rightarrow {}^{208}\mathrm{Pb} + {}^{24}\mathrm{Ne}$, shown in Figure 1.3. Nuclei nearer the closed shell of ^{208}Pb, and with correspondingly smaller clusters, have spectra with more evenly spaced levels like the vibrational model. Yet smaller clusters compress the energy levels further and can even result in the higher levels of the $J^\pi = 0^+, 2^+, 4^+ \ldots$ band becoming inverted, as with the 18^+ level in $^{212}\mathrm{Po} \rightarrow {}^{208}\mathrm{Pb} + \alpha$ [9], illustrated in Figure 1.3.

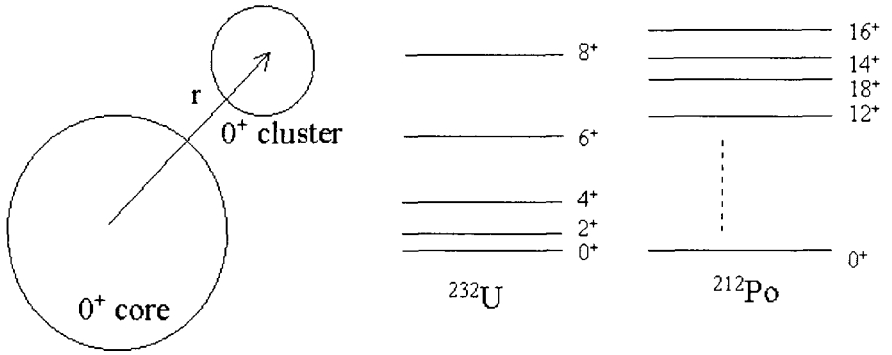

Figure 1.3: *Spectra generated by the binary cluster model.*

Of interest also is the expectation that, if energetically allowed, there will be a decay mode in which the products are the cluster and core, for instance $^{8}\mathrm{Be} \rightarrow \alpha + \alpha$. Alpha decay is a very common decay mode and much work has been done using an alpha particle as the cluster. The alpha cluster model has been successfully applied throughout the Periodic Table [10, 11, 12]. The exotic decay of heavy nuclei is also extremely interesting in this context, as energetically there is the possibility of the emission of various heavier clusters. Buck et al. [13] have obtained good fits to exotic decay half lives involving clusters like $^{14}\mathrm{C}$, $^{24}\mathrm{Ne}$ and $^{28}\mathrm{Mg}$. Nuclear decay in the cluster model will be discussed in detail in Chapter 3.

The possibility of more than two nucleon groups has also been investigated and the similarities to molecular interactions examined [14, 15]. However multiple cluster states are outside the scope of this thesis and we limit ourselves to the binary cluster model.

Chapter 2

The Cluster Model: An overview

> "We consider that a cluster in a nuclear system is a spatially localized subsystem composed of strongly correlated nucleons. The clustering correlation is, therefore, defined as one which acts to form a spatially localized cluster. ... the cluster model proves its merits when the clustering correlation is so strong that the well-developed cluster structure [is] realized, where the relative motion between the clusters becomes the fundamental mode of motion of the nucleus. Therefore, the spatial localization of [the] subsystem and the relative motion between these subsystems give us the clear concept of the well developed cluster structure." –Kiyomi Ikeda [14]

In order to implement any form of the binary cluster model, the appropriate core-cluster decomposition of a given nucleus must be determined, the interaction between the core and cluster specified, and the quantum numbers of the relative motion between the core and cluster assigned. Once this has been accomplished quantities generated from the model can be compared to experiment, for example, the energies E_{nL} and electric transition strengths B(Eℓ).

2.1 Core-cluster decomposition

The binary decomposition of a nucleus $[A, Z]$ involves defining a core $[A_1, Z_1]$ and a cluster $[A_2, Z_2]$*. In real systems the boundary between the core and the cluster will probably be fuzzy. A superposition of many core-cluster configurations is likely to exist. However the most prominent configuration should provide a reasonable approximation to such a superposition. The specific breakdown into core and cluster can be deduced from the various independent methods briefly introduced below. Agreement between their results provides good evidence that clustering does occur.

Most heavy nuclei undergo alpha decay but occasionally a decay with a more massive ejectile is observed. The exotic decay products have been found to provide good candidates for core-cluster partitions, using the daughter as the core and the ejectile as the cluster. This method was used by Buck et al. [13] in their early work on heavy

*where $A = A_1 + A_2$ and $Z = Z_1 + Z_2$

clusters, enabling them to satisfactorily reproduce the exotic decay half lives, the spectra and the B(E2) values. The cluster is considered to be preformed within the nucleus and the probability of it penetrating the Coulomb barrier can be calculated. Some nuclei have multiple decay modes, suggesting the existence of multiple core-cluster decompositions. In Chapter 3, the core-cluster decompositions deduced from exotic decay will be discussed and a comparison made between the experimental and theoretical decay constants.

The likelihood of a particular cluster forming within a nucleus should also depend on the stability of the cluster in question. In fact the stability of the both the cluster and the core is important, so that "the best balance of cluster and core individual binding energies is needed" [16]. The best combination is given by maximising the difference between an average binding energy, calculated using the liquid drop formula, and the actual binding energy. The BMHP method developed by Buck et al. [16, 17] will be described in detail in Chapter 4.

Energy spectra are a source of structural information and can be used to deduce core-cluster configurations. Spectra obtained from applications of the cluster model depend strongly on the core-cluster decomposition (see Figure 1.3). Thus the specific cluster that most closely reproduces the experimental spectra for a given nucleus provides the most likely decomposition. In Chapter 5 we discuss this method of finding the optimum partition of the nucleus.

2.2 Core-cluster interaction

In the binary cluster model the Hamiltonian separates into terms corresponding to the centre of mass and relative motion. The Schrodinger equation for the relative motion is given by[†]

$$\hat{H}\Psi(\vec{r}) = \left[-\frac{\hbar^2}{2\mu}\nabla^2 + V(\vec{r})\right]\Psi(\vec{r}) = E\Psi(\vec{r}). \tag{2.1}$$

Taking a central interaction $V(\vec{r}) = V(r)$ and replacing the total kinetic energy by its radial and rotational components separates Eq. (2.1) into radial and angular parts. Thus, substituting $\Psi(\vec{r}) = \frac{1}{r}\psi_{nL}(r)Y_{LM}(\theta,\phi)$, we find

$$\left[-\frac{\hbar^2}{2\mu}\frac{1}{r}\frac{\mathrm{d}^2}{\mathrm{d}r^2}r + \frac{\vec{l}^2}{2\mu r^2} + V(r)\right]\frac{\psi_{nL}(r)}{r}Y_{LM}(\theta,\phi) = E_{nL}\frac{\psi_{nL}(r)}{r}Y_{LM}(\theta,\phi). \tag{2.2}$$

Using the eigenvalue equation for the angular momentum operator, $\vec{l}^2 Y_{LM}(\theta,\phi) = \hbar^2 L\,(L+1)\,Y_{LM}(\theta,\phi)$, premultiplying by $Y^*_{LM}(\theta,\phi)$ and integrating over the angles, leads to the radial Schrodinger equation:

$$\left[-\frac{\hbar^2}{2\mu}\frac{\mathrm{d}^2}{\mathrm{d}r^2} + \frac{\hbar^2 L\,(L+1)}{2\mu r^2} + V(r)\right]\psi_{nL}(r) = E_{nL}\psi_{nL}(r). \tag{2.3}$$

[†]Where $\mu = \frac{A_1 A_2}{A_1 + A_2}$ is the reduced mass of the system.

In Eq. (2.3) n is the number of nodes and L the orbital angular momentum quantum number.

In this thesis, we employ the simpler semi-classical integral form of the radial Schrodinger equation, given by the Bohr-Sommerfeld quantization rule,

$$\int_{r_1}^{r_2} \mathrm{d}r \sqrt{\frac{2\mu}{\hbar^2}\left[E_{nL} - V(r,R)\right]} = (2n+1)\frac{\pi}{2}. \tag{2.4}$$

The potential $V(r,R)$ in Eq. (2.4) contains nuclear, Coulomb and Langer-modified centrifugal terms:

$$V(r,R) = V_N(r,R) + V_C(r,R) + \frac{\hbar^2}{2\mu r^2}\left(L+\frac{1}{2}\right)^2. \tag{2.5}$$

The Coulomb potential $V_C(r,R_C)$ is given the form appropriate to a uniformly charged spherical core (radius R_C) and a point cluster,

$$V_C(r,R_C) = \begin{cases} \frac{Z_1 Z_2 e^2}{r} & r \geq R_C \\ \frac{Z_1 Z_2 e^2}{2R_C}\left[3 - \left(\frac{r}{R_C}\right)^2\right] & r \leq R_C. \end{cases} \tag{2.6}$$

To reduce the number of variables in the potential the nuclear and the Coulomb potential radii are set as equal, so $R_C = R$.

In the development of the binary cluster model various forms have been used for the nuclear potential $V_N(r,R)$. Initially Buck et al. [18, 10] used a square well and a simplified "surface-charge" Coulomb potential: $V = -V_N + C/R$ $(r < R)$, $V = C/r$ $(r > R)$. $C = Z_1 Z_2 e^2$. They achieved good agreement with a large number of alpha-decay half-lives in strong support of their alpha cluster model. A more realistic description of the potential involved the use of a hyperbolic cosine [19]

$$V_N(r,R) = -V_0 \frac{1+\cosh(R/a)}{\cosh(r/a)+\cosh(R/a)} \tag{2.7}$$

and the more sophisticated Coulomb potential of Eq. (2.6). For large R/a this potential has a similar shape to the Saxon Woods nuclear potential described in Chapter 1. However the standard form of the Saxon Woods potential was found not to reproduce the anomalously large back-angle scattering of alpha particles by closed shell nuclei; and Michel et al. [11] and Buck et al. [7, 20] were led to use variations which reproduced this scattering. The real part of Michel's nuclear potential involves a Saxon Woods squared form

$$V(r) = -V_0 \frac{1+\alpha\exp\left[-\left(\frac{r}{\rho}\right)^2\right]}{\left\{1+\exp\left[\frac{r-R_R}{2a_R}\right]\right\}^2} \tag{2.8}$$

which

"proves successful in describing the complicated evolution of the angular distribution pattern, including the backward enhancement observed at low energies as well as its progressive disappearance with increasing energy." –Francis Michel et al. [11]

The nuclear potential to be used in this work is the variation of Buck et al., a mixture of Saxon Woods and Saxon Woods cubed forms given by

$$V_N(r,R) = -V_0 f(r,R,a,x) \tag{2.9}$$

where

$$f(r,R,a,x) = \frac{x}{1+\exp\left[\frac{r-R}{a}\right]} + \frac{1-x}{\left\{1+\exp\left[\frac{r-R}{3a}\right]\right\}^3}, \tag{2.10}$$

with x a mixing parameter. In dealing with clusters of different mass A_2, the potential strength V_0 in Eq. (2.9) was originally taken to be proportional to A_2 so that

$$V_0 = U_0 A_2 \tag{2.11}$$

with $U_0 \approx 50$ MeV. Such a potential is not symmetric with respect to the interchange of core and cluster, whereas a symmetric potential would be more physical. Thus Buck et al. [21] introduced a mass symmetric potential

$$V_N(r,R) = -\left(\frac{A_1 A_2}{A_1+A_2}\right) U_0 \frac{f(r,R,a,x)}{f(0,R,a,x)} \tag{2.12}$$

with the $f(r,R,a,x)$ as defined in Eq. (2.10). The difference in shape between this potential (Eq. (2.12)) and the Saxon-Woods potential is illustrated in Figure 2.1.

2.3 Core-cluster orbit quantum numbers

The Pauli principle prohibits the nucleons in the cluster from occupying the same states as the nucleons in the core. This effect is approximated in the cluster model by ensuring appropriately surface peaked core-cluster wavefunctions by a suitable choice of the global quantum number $G = 2n + L$, which characterises the band with $J^\pi = L^\pi = 0^+, 2^+, 4^+, \ldots G^+$. Here n is the number of nodes in the wave function and L is the angular momentum of a state in that G-band. The Bohr-Sommerfeld relation of Eq. (2.4) becomes

$$\int_{r_1}^{r_2} \mathrm{d}r \sqrt{\frac{2\mu}{\hbar^2}\left[E_{nL} - V(r,R)\right]} = (G - L + 1)\frac{\pi}{2}. \tag{2.13}$$

The Wildermuth condition, which maintains the total number of oscillator quanta independently of the mode of partition of the system, can be applied to estimate a value for G. For example, consider a system comprised of a closed-shell core plus some valence nucleons such as ${}^{228}_{90}\mathrm{Th}^{138}$. The last closed shell is ${}^{208}_{82}\mathrm{Pb}^{126}$, so there are 8 valence protons in the $g = 5$ shell and 12 valence neutrons in the $g = 6$ shell, thus the total number of valence quanta is 112. If the valence nucleons are grouped together into a cluster and

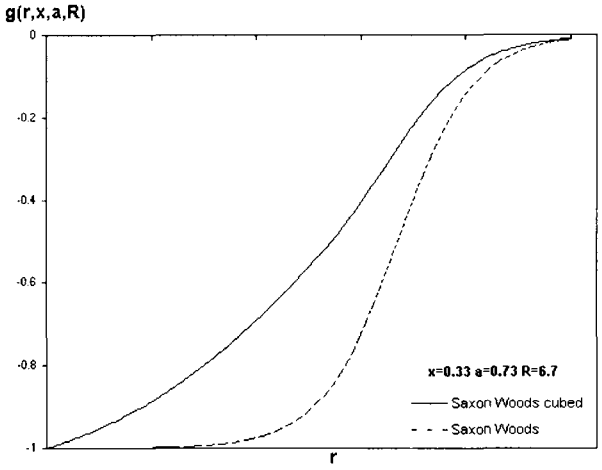

Figure 2.1: *The ordinary Saxon Woods potential is closer to the square form compared to a similarly normalised Saxon Woods & Saxon Woods cubed potential,* $g(r,x,a,R) = \frac{f(r,R,a,x)}{f(0,R,a,x)}$ *with* $x = 0.33$*.* $R = 6.7\,fm$ *and* $a = 0.73\,fm$ *in both cases.*

the total number of quanta are recalculated, any difference is attributed to the cluster's relative motion with the core. Now consider the core-cluster configuration

$$^{228}_{90}\mathrm{Th}^{138} \rightarrow {}^{208}_{82}\mathrm{Pb}^{126} + {}^{20}_{8}\mathrm{O}^{12} \tag{2.14}$$

where the valence nucleons are grouped into ^{20}O which has 8 protons: 2 in the $g = 0$ shell and 6 in the $g = 1$ shell; then there are the 12 neutrons: 2 in $g = 0$, 6 in $g = 1$ and 4 in the $g = 2$ shell. So in total ^{20}O has 20 quanta. There is thus a deficit in valence quanta of $112 - 20 = 92$ quanta, so $G = 92$, which also corresponds to the maximum orbital angular momentum L of the core-cluster relative motion.

This condition is only a guide, in that the simple harmonic oscillator description neither takes into account the spin-orbit interaction which significantly shifts the single-particle energies, nor the variation in the oscillator frequency for core and cluster due to their large mass difference. For heavy nuclei Buck et al. have used a simple prescription for G based roughly on the Wildermuth condition, scaling it with the cluster mass such that

$$G = gA_2 \tag{2.15}$$

where $g = 5$ in the actinide region and $g = 4$ for the rare earth region [22, 23, 24]. In the case above G would be $5 \times 20 = 100$ slightly larger than the value obtained using the Wildermuth condition.

Some investigations have been done using a G that is symmetric with respect to the interchange of core and cluster. This becomes important when the clusters become large and comparable in size to the core, as is the case in the cluster model interpretation of superdeformation. When applying the binary cluster model to superdeformation

Buck et al. [25] developed an expression for G by examining the scaling with A_1A_2 of the Bohr-Sommerfeld quantization rule, Eq. (2.13). They found

$$G = \frac{0.88A_1A_2}{(A_1 + A_2)^{2/3}} = 0.88\mu\,(A_1 + A_2)^{1/3}\,. \tag{2.16}$$

G is then rounded off to the nearest even integer. These prescriptions for G will be explored further in Chapter 3.

2.4 B(Eℓ) values

The coupling between an electromagnetic field and the nucleons within the nucleus can result in a transition between an initial and a final state of a nucleon (mass m_i, charge q_i) at position (r_i, θ_i, ϕ_i) in the nucleus. The transition is accompanied by the emission (or absorption) of radiation. Electric transitions, which are of interest here, are induced by the operator

$$\hat{B} = \sum_i q_i r_i^\ell Y^*_{\ell m}(\theta_i, \phi_i) \tag{2.17}$$

where ℓ is the angular momentum transfer between the field and the system of charges [26]. If the final state is spinless, for instance the ground state of an even-even nucleus, then the probability of a transition is related to the transition strength B(Eℓ)[‡], where

$$\begin{aligned} \mathrm{B(E}\ell) &= \left|\left\langle \Psi_{00} \left| \hat{B} \right| \Psi_{\ell m} \right\rangle\right|^2 \\ &= \left|\left\langle \Psi_{00} \left| \sum_i q_i r_i^\ell Y^*_{\ell m}(\theta_i, \phi_i) \right| \Psi_{\ell m} \right\rangle\right|^2 . \end{aligned}$$

Specializing the above to the binary cluster model of the nucleus, the core and cluster make up a two charge distribution, Z_1 and Z_2, and thus

$$\hat{B} = Z_1 r_1^\ell Y^*_{\ell m}(\theta_1, \phi_1) + Z_2 r_2^\ell Y^*_{\ell m}(\theta_2, \phi_2). \tag{2.18}$$

In the centre of mass frame the transition strength can be written in terms of the relative coordinate only, see Figure 2.2.

$$\begin{aligned} \mathrm{B(E}\ell) &= \left|\frac{1}{\sqrt{4\pi}} \left\langle \frac{\psi_0(r)}{r} \right| Z_1 r_1^\ell Y^*_{\ell m}(\pi - \theta, \pi + \phi) + Z_2 r_2^\ell Y^*_{\ell m}(\theta, \phi) \left| \frac{\psi_\ell(r)}{r} Y_{\ell m}(\theta, \phi) \right\rangle\right|^2 \\ &= \frac{1}{4\pi} \left|\left\langle \frac{\psi_0(r)}{r} \right| Y^*_{\ell m}(\theta, \phi) \left\{ (-1)^\ell Z_1 r_1^\ell + Z_2 r_2^\ell \right\} \left| \frac{\psi_\ell(r)}{r} Y_{\ell m}(\theta, \phi) \right\rangle\right|^2 \end{aligned}$$

Converting to the relative coordinate r, where $r_1 = \frac{A_2 r}{A}$ and $r_2 = \frac{A_1 r}{A}$,

[‡]Throughout this thesis we use notation B(Eℓ) = B(E$\ell\downarrow$) = B(E$\ell : \ell \to 0^+$).

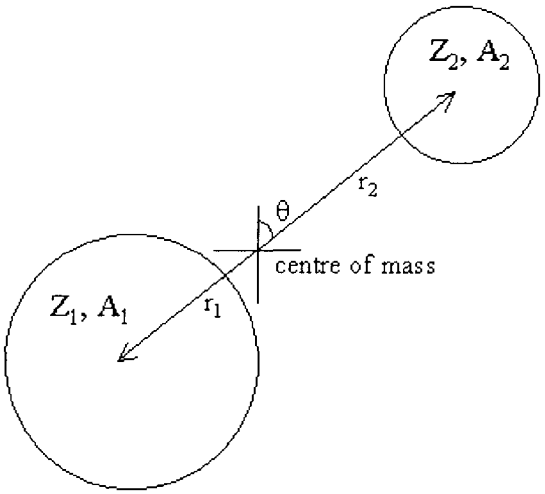

Figure 2.2: *Schematic representation of the core-cluster coordinates of relative motion.*

$$\begin{aligned}
\mathrm{B(E}\ell) &= \frac{1}{4\pi}\left|\left\langle \frac{\psi_0(r)}{r}\right| Y^*_{\ell m}(\theta,\phi)\left\{(-1)^\ell Z_1\left(\frac{A_2 r}{A}\right)^\ell + Z_2\left(\frac{A_1 r}{A}\right)^\ell\right\}\left|\frac{\psi_\ell(r)}{r}Y_{\ell m}(\theta,\phi)\right\rangle\right|^2 \\
&= \frac{1}{4\pi}\left|\left\langle \frac{\psi_0(r)}{r}\right| Y^*_{\ell m}(\theta,\phi) r^\ell\left\{Z_1\left(\frac{-A_2}{A}\right)^\ell + Z_2\left(\frac{A_1}{A}\right)^\ell\right\}\left|\frac{\psi_\ell(r)}{r}Y_{\ell m}(\theta,\phi)\right\rangle\right|^2 \\
&= \frac{1}{4\pi}\left|\int_0^\infty \frac{\psi^*_0(r)}{r}\left\{Z_1\left(\frac{-A_2}{A}\right)^\ell + Z_2\left(\frac{A_1}{A}\right)^\ell\right\} r^\ell \frac{\psi_\ell(r)}{r} r^2 \mathrm{d}r\right|^2 .
\end{aligned}$$

The transition probabilities decrease rapidly with multipolarity [6], and here we concentrate on:

1. Dipole transitions: $\ell = 1$
2. Quadrupole transitions: $\ell = 2$.

2.4.1 Dipole transitions

For a spinless final state the binary cluster B(E1) value is given by

$$\mathrm{B(E1)} = \frac{1}{4\pi}\left|\left\{Z_1\left(\frac{-A_2}{A}\right) + Z_2\left(\frac{A_1}{A}\right)\right\}\int_0^\infty \psi^*_0(r) r \psi_1(r)\mathrm{d}r\right|^2 . \tag{2.19}$$

The very small B(E1) values observed (see ref. [27]) for transitions between low-lying states of opposite parity in heavy nuclei imply that

$$Z_1\left(\frac{-A_2}{A}\right) + Z_2\left(\frac{A_1}{A}\right) = 0 \tag{2.20}$$

which leads to the no dipole condition

$$Z_1 A_2 = Z_2 A_1. \tag{2.21}$$

As $Z = Z_1 + Z_2$ and $A = A_1 + A_2$ we get

$$\frac{Z}{A} = \frac{Z_1}{A_1} = \frac{Z_2}{A_2}. \tag{2.22}$$

This condition is very important in the application of the model especially when obtaining the core-cluster decomposition.

2.4.2 Quadrupole transitions

Similarly, for a spinless final state the binary cluster B(E2) value is given by

$$\mathrm{B(E2)} = \frac{1}{4\pi}\left|\left\{Z_1\left(\frac{A_2}{A}\right)^2 + Z_2\left(\frac{A_1}{A}\right)^2\right\}\int_0^\infty \psi_0^*(r) r^2 \psi_2(r)\mathrm{d}r\right|^2 \tag{2.23}$$

Applying the no-dipole condition we can rewrite the expression

$$\begin{aligned} Z_1\left(\frac{A_2}{A}\right)^2 + Z_2\left(\frac{A_1}{A}\right)^2 &= Z_1\left(\frac{Z_2}{Z}\right)\left(\frac{A_2}{A}\right) + Z_2\left(\frac{Z_1}{Z}\right)\left(\frac{A_1}{A}\right) \\ &= \frac{Z_1 Z_2}{Z}\left(\frac{A_1 + A_2}{A}\right) \\ &= \frac{Z_1 Z_2}{Z}, \end{aligned}$$

and thus

$$\mathrm{B(E2)} = \frac{1}{4\pi}\left|\frac{Z_1 Z_2}{Z}\int_0^\infty \psi_0^*(r) r^2 \psi_2(r)\mathrm{d}r\right|^2. \tag{2.24}$$

A characteristic of the cluster model for heavy nuclei is that the multinodal radial wavefunctions ψ_0 and ψ_2 are very similar in the important surface region [28]. Thus

$$\mathrm{B(E2)} \approx \frac{1}{4\pi}\left|\frac{Z_1 Z_2}{Z}\int_0^\infty \psi_0^*(r) r^2 \psi_0(r)\mathrm{d}r\right|^2 \tag{2.25}$$

$$\approx \frac{1}{4\pi}\left|\frac{Z_1 Z_2}{Z} r_0^2 A^{2/3}\right|^2. \tag{2.26}$$

This relationship is informative and a good test of the binary cluster model. When the cluster charge Z_2 is large then the transitions are strongly enhanced compared to $Z_2 \sim 1$ which corresponds to single-particle-like transitions. Chapter 6 will explore this relationship in further detail.

Chapter 3

Nuclear Decay

3.1 Background

The studies of radioactive decay by Becquerel and the Curies caught Rutherford's attention, and his investigations of the nature of radioactivity led to a Nobel prize for chemistry in 1908. He worked primarily on the emission of alpha particles, which he concluded were the nuclei of Helium atoms [1].

> "It is very remarkable that a chemically inert element like helium should play such a prominent part in the constitution of the atomic systems of uranium and thorium and radium" –Ernest Rutherford [29]

"Emission is a Coulomb repulsion effect" [6] as the particle emitted has to tunnel through the Coulomb barrier, and for this to occur spontaneously the mass of the daughter-ejectile system must be less than that of the parent. The energy thus liberated appears as kinetic energy of the fragments and is known as the Q-value, where

$$Q = \left[m_{\text{parent}} - \left(m_{\text{daughter}} + m_{\text{ejectile}}\right)\right] c^2. \tag{3.1}$$

So, if on average the nucleons within the daughter-ejectile system are more tightly bound than in the corresponding parent system then the Q-value is positive and spontaneous emission can occur. The alpha particle is particularly tightly bound and has a small charge compared to larger ejectiles, thus lessening the Coulomb barrier. Therefore alpha decay is the dominant decay mode for heavy nuclei.

The possibility of emission of particles heavier than alpha-particles was only considered in the early 1980's, when Sandulescu et al. predicted "in the region $Z \geq 88$ 'a new type of decay which can be interpreted as ... emission of a heavy cluster.' " [30] Due to shell effects, they listed a selection of nuclei that may exhibit exotic decay in observable competition to alpha decay. Rose and Jones [31] recorded the first experimental evidence of such exotic decay. Although they had multiple problems, they observed eight definite events of the emission of ^{14}C from ^{223}Ra during a 194 day run. The rarity of such emission prompted a rather disparaging review [32] of their findings—however further studies confirmed their result and revealed more exotic decay modes, for example the decay of

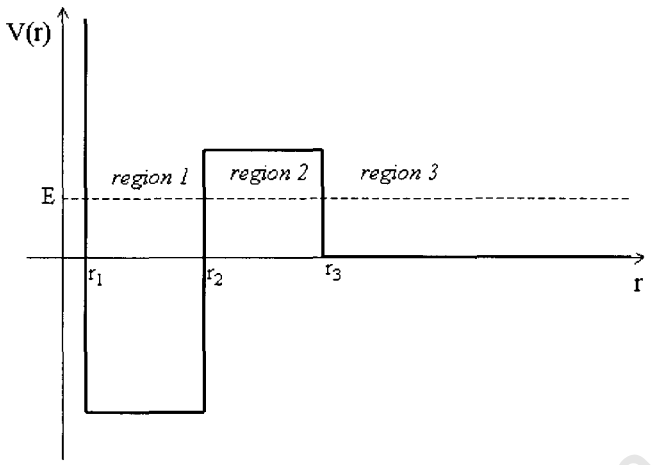

Figure 3.1: *A simple square well potential barrier, indicating the regions where a classical particle is allowed (regions 1 and 3) and forbidden (region 2).*

^{232}U by ^{24}Ne [33].

A fundamental premise in cluster models is the non-zero probability of the emitted particle being preformed within the parent nucleus. Sandulescu et al. [30] originally believed, as exotic decay had not been observed at that time, that the probability of the preformation of large clusters compared to alphas was too small for heavy cluster emission to be observed. Calculations of preformation factors are very complex and the cluster model of Buck et al. [19, 18] assumes this preformation factor to be unity, simplifying the decay constant calculations with no observable adverse effect as yet.

3.2 Half-lives and Decay constants

The theoretical quantum mechanical basis for the calculation of decay constants, and thus half-lives, was developed by Gamow and Gurney in 1928 [6]. Before the advent of quantum mechanics alpha decay posed an insurmountable problem, as disintegration occurred without the addition of energy into the system. Classically a particle initially bound within some potential, $V(\vec{r})$, was bound there permanently. In the then new quantum theory Gurney and Condon discuss the finite probability of a particle tunneling through the potential barrier, "this gives us at last a nucleus which can disintegrate without the absorption of energy." [34].

The decay laws can be simply derived with a semi-classical treatment using the simple potential in Figure 3.1. The probability of decay per unit time or the disintegration constant is $\lambda = fP$, where f is the frequency of the assault of the ejectile on the barrier and P the probability of transmission through the barrier on each attempt. The half-life

is then

$$\mathrm{T}_{\frac{1}{2}} = \frac{\ln 2}{\lambda} = \frac{\ln 2}{fP}. \tag{3.2}$$

Now

$$\frac{1}{f} = \frac{2(r_2 - r_1)}{v} = \frac{2m(r_2 - r_1)}{p} = \frac{2m(r_2 - r_1)}{\hbar K} = \frac{2m}{\hbar}\int_{r_1}^{r_2}\frac{dr}{K} \tag{3.3}$$

where v, p and K are the (constant) velocity, momentum and wave-number, in the classically allowed region between r_1 and r_2.

The probability of tunneling through the barrier, for a single approach, is given by the ratio of the probability densities at the edges of the barrier,

$$\frac{(\psi\psi^*)_{transmitted}}{(\psi\psi^*)_{incident}}. \tag{3.4}$$

For an infinitely thick barrier only the exponentially decreasing term of the wave function persists so, taking the barrier thickness to be large [35], the transmission probability is

$$\mathrm{P} = \exp\{-2k(r_3 - r_2)\} = \exp\left\{-2\int_{r_2}^{r_3} k dr\right\} \tag{3.5}$$

where k is the wave number in region 3. Thus

$$\mathrm{T}_{\frac{1}{2}} = \frac{2m\ln 2}{\hbar}\left[\int_{r_1}^{r_2}\frac{dr}{K}\right]\left[\exp\left\{2\int_{r_2}^{r_3} k dr\right\}\right]. \tag{3.6}$$

For more complex potentials the wave numbers K and k are functions of r, and r_1, r_2 and r_3 correspond to the classical turning points defining the allowed and forbidden regions, so

$$\mathrm{T}_{\frac{1}{2}} = \frac{2m\ln 2}{\hbar}\left[\int_{r_1}^{r_2}\frac{dr}{K(r)}\right]\left[\exp\left\{2\int_{r_2}^{r_3} k(r) dr\right\}\right]. \tag{3.7}$$

The decay constant is then

$$\lambda = \frac{\ln 2}{\mathrm{T}_{\frac{1}{2}}} \tag{3.8}$$

$$= \frac{\hbar}{2m}\frac{\exp\left\{-2\int_{r_2}^{r_3} k(r) dr\right\}}{\int_{r_1}^{r_2}[K(r)]^{-1} dr}, \tag{3.9}$$

and the decay width $\Gamma = \hbar\lambda$. Eq. (3.7) and (3.9) are also obtained using a rigorous quantum mechanical treatment of decay [36, 18].

The decay constants are especially sensitive to relatively small variations in Q-value. As decay is essentially a Coulomb barrier problem, the effect of the electron cloud as the ejectile escapes the atom is not negligible. Thus the Q-value needs to be increased by the electron shielding correction [37, 38],

$$Q_{es} = 32.6 Z_2 (Z_1 + Z_2)^{7/5} \text{ eV}. \tag{3.10}$$

Using the cluster model potentials described in Chapter 2, decay constants can be computed by performing the integrations of Eq. (3.9). The difference between the corrected Q-value and the potential $V(r, R)$ from Eq. (2.5) is zero at the boundaries of the classically forbidden region, thus defining the integral limits r_1. r_2, and r_3. (See Figure 3.2.)

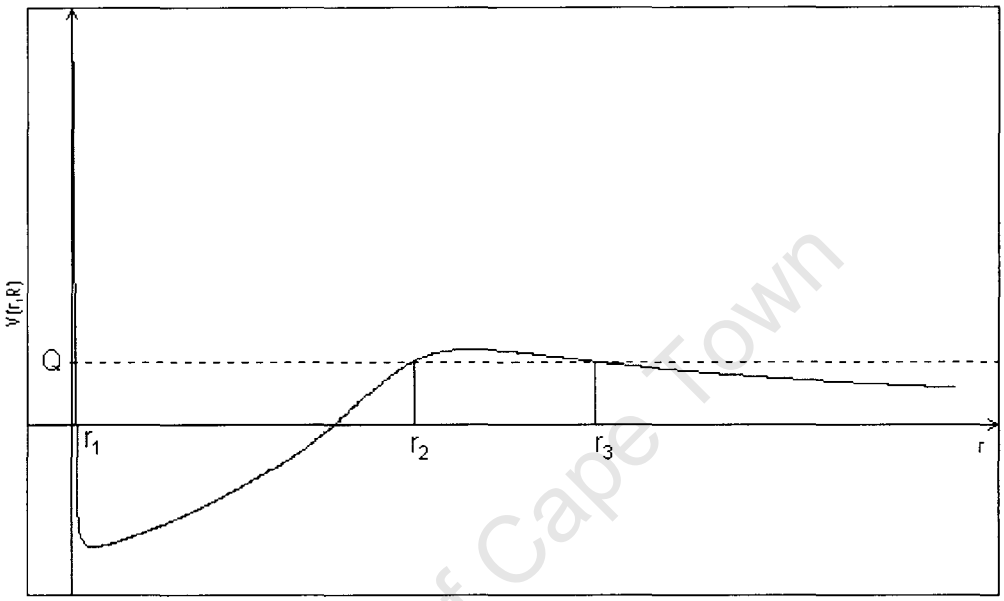

Figure 3.2: *The characteristic form of the core-cluster potential, $V(r, R)$, of Eq. (2.5), together with the three turning points (r_1, r_2, r_3) for a particular Q-value, Q.*

3.3 Fits to most recent data and deduced core-cluster decompositions.

An exotic decay analysis similar to that of Buck et al. [13] is implemented here using a more extensive and accurate data set [39, 40, 41]. Calculations have been performed using both the asymmetric and symmetric potential described in Section 2.2. The method for calculating the decay constants is best described by considering first the asymmetric potential. We retained the 'geometrical' potential parameter values used by Buck et al. [13] to reduce the number of free parameters, so $G = 5A_2$, $x = 0.36$ and $a = 0.75$ fm. Starting with an initial guess for the potential depth U_0, values for R and the classical turning points (r_1, r_2, r_3) were found using the Bohr-Sommerfeld relation Eq. (2.13) and the relevant Q-value (or ground state energy, E_{n0}) for each nucleus. The decay constants of Eq. (3.9) were then calculated, and compared to experimental values. The goodness of fit parameter was defined as

$$S = \sum_i \left[\frac{(\ln \lambda_i(theory)) - (\ln \lambda_i(exp))}{\Delta\lambda_i(exp)/\lambda_i(exp)} \right]^2, \tag{3.11}$$

where $\lambda_i(exp)$ are the experimentally determined values of the decay constants and $\Delta\lambda_i(exp)$ the corresponding errors. The potential depth U_0 was adjusted and the method iterated so that S in Eq. (3.11) was minimised and the fit optimised.

There is an ambiguity in the experimental data for ^{234}U and ^{238}Pu where the preferred choice of ejectile out of two possibilities is not clear. Thus ^{234}U could decay via ^{24}Ne and/or ^{26}Ne and the decay of ^{238}Pu could be via ^{28}Mg and/or ^{30}Mg. Our results in Table 3.1 indicate our calculations do not discriminate between these possibilities at a level of a factor of two, and both clusters were included in the fitting procedure. A resulting potential depth of $U_0 = 55.7$ MeV produced excellent fits, with $S = 169$ and the majority of the values within a factor of two of the corresponding measurements. The decay constants are listed in Table 3.1.

A similar analysis using the symmetric potential was also done, again limiting the number of free parameters by using previously defined values $G = 5A_2$, $x = 0.33$ and $a = 0.73$ fm [21]. Optimisation yielded $U_0 = 56.2$ MeV, with $S = 899$. This is an abysmal fit, with a number of decay constants more than an order of magnitude out. This problem, although perceived by Buck et al. [21], was not rectified by them. An inconsistency in their approach is noted here: symmetrisation was limited to the potential only, whereas the global quantum number, G, remained in the asymmetric form of Eq. (2.15). Once a complete symmetric treatment* is used with G from Eq. (2.16), then the fits are markedly better with $U_0 = 52.9$ MeV, $S = 178$. Table 3.1 also lists the resulting decay constants compared to experimental values.

It is surprising to note that even though the values of the nuclear radius, R, are fitted they show very little variation. Buck et al. have found similar results in their extensive application of the cluster model in the rare-Earth region [24]. For the 43 nuclei with $150 \leq A \leq 190$ their results for R fall in the narrow range $R = 5.73 \pm 0.10$ fm, with no evident $A^{1/3}$ dependence. On traversing the closed shell at ^{208}Pb the value of R increases sharply. The consistency of R throughout a major shell is an interesting feature of the model that requires further probing.

Table 3.1 demonstrates the ability of the model to successfully reproduce decay constants. It also provides a simple prescription for choosing the core-cluster decomposition, i.e. the literal separation of the parent into a daughter and ejectile.

*The symmetric potential's shape parameters remain unchanged with $x = 0.33$ and $a = 0.73$ fm.

Decay	Asymmetric potential		Symmetric potential		λ(exp)[s^{-1}]
	R [fm]	λ(theory)[s^{-1}]	R [fm]	λ(theory)[s^{-1}]	
$^{222}Ra \rightarrow {}^{208}Pb + {}^{14}C$	6.6189	5.13×10^{-12}	6.7733	9.08×10^{-12}	$(4.18 \pm 0.55) \times 10^{-12}$
$^{224}Ra \rightarrow {}^{210}Pb + {}^{14}C$	6.6449	7.90×10^{-17}	6.8015	1.50×10^{-16}	$(1.45 \pm 0.22) \times 10^{-16}$
$^{226}Ra \rightarrow {}^{212}Pb + {}^{14}C$	6.6687	6.30×10^{-22}	6.8271	1.24×10^{-21}	$(3.99 \pm 1.38) \times 10^{-22}$
$^{228}Th \rightarrow {}^{208}Pb + {}^{20}O$	6.5849	2.01×10^{-22}	6.7254	2.29×10^{-22}	$(1.32 \pm 0.26) \times 10^{-21}$
$^{230}Th \rightarrow {}^{206}Hg + {}^{24}Ne$	6.6097	2.75×10^{-25}	6.7484	2.19×10^{-25}	$(1.70 \pm 0.30) \times 10^{-25}$
$^{230}U \rightarrow {}^{208}Pb + {}^{22}Ne$	6.6775	4.60×10^{-21}	6.8756	1.31×10^{-20}	$(1.82 \pm 1.02) \times 10^{-20}$
$^{232}U \rightarrow {}^{208}Pb + {}^{24}Ne$	6.6085	2.80×10^{-21}	6.7431	2.08×10^{-21}	$(2.64 \pm 0.28) \times 10^{-21}$
$^{234}U \rightarrow {}^{210}Pb + {}^{24}Ne$	6.6291	1.48×10^{-26}	6.7641	1.12×10^{-26}	$(8.33 \pm 6.07) \times 10^{-27}$
$^{234}U \rightarrow {}^{208}Pb + {}^{26}Ne$	6.5749	4.97×10^{-27}	6.7488	7.23×10^{-27}	$(8.33 \pm 6.07) \times 10^{-27}$
$^{234}U \rightarrow {}^{206}Hg + {}^{28}Mg$	6.6398	6.89×10^{-26}	6.7932	4.99×10^{-26}	$(5.02 \pm 0.91) \times 10^{-26}$
$^{236}Pu \rightarrow {}^{208}Pb + {}^{28}Mg$	6.6374	1.04×10^{-21}	6.7860	6.82×10^{-22}	$(2.09 \pm 0.54) \times 10^{-22}$
$^{238}Pu \rightarrow {}^{210}Pb + {}^{28}Mg$	6.6561	1.18×10^{-26}	6.8046	7.81×10^{-27}	$(1.38 \pm 0.97) \times 10^{-26}$
$^{238}Pu \rightarrow {}^{208}Pb + {}^{30}Mg$	6.6107	2.53×10^{-26}	6.7249	6.02×10^{-27}	$(1.38 \pm 0.97) \times 10^{-26}$
$^{238}Pu \rightarrow {}^{206}Hg + {}^{32}Si$	6.6681	3.83×10^{-26}	6.8474	3.35×10^{-26}	$(3.72 \pm 1.35) \times 10^{-26}$
$^{242}Cm \rightarrow {}^{208}Pb + {}^{34}Si$	6.6374	3.93×10^{-24}	6.7845	1.25×10^{-24}	$(4.95 \pm 1.42) \times 10^{-24}$

Table 3.1: *Decay constants, calculated using the asymmetric potential ($G = 5A_2$, $a = 0.75$ fm, $x = 0.36$, $U0 = 55.7$ MeV, $S = 169$), and the symmetric potential (G from Eq. (2.16), $a = 0.73$ fm, $x = 0.33$, $U0 = 52.9$ MeV, $S = 178$) , compared to the corresponding experimental values. [39, 40, 41]*

Chapter 4

The Maximum Stability Hypothesis

4.1 Connection with exotic decay

In the previous section core-cluster decompositions were obtained from exotic decay data. The applicability of this is limited to the nuclei with known exotic decays. However the systematics of these exotic decays hold the key to finding the likely core-cluster decompositions for other nuclei. Out of the fifteen exotic decay modes known (listed in Table 3.1), eight have $^{208}_{82}\mathrm{Pb}^{126}$ as the daughter, which is doubly magic. All the other daughters and a further five of the ejectiles are magic. This shows a clear tendency for the core and/or the cluster to be more tightly bound than on average. Drawing from these observations, a generally applicable method for determining the core-cluster decompositions is presented.

4.2 Multi-cluster BMHP technique

"The optimal decomposition is not at all obvious" - Brian Buck et al. [16]

In a relatively simple prescription, Buck et al. developed a method of determining the most likely decomposition, using differences between actual and average binding energies. For an arbitary nucleus an indicator of its relative stability is

$$D = B_A(Z, A) - B_L(Z, A) \tag{4.1}$$

where $B_A(Z, A)$ is the actual binding energy of the nucleus and $B_L(Z. A)$ is the theoretical binding energy given by the liquid drop formulation [42]:

$$B_L = a_v A - a_s A^{2/3} - a_c \frac{Z^2}{A^{1/3}} - a_a \frac{(A-2Z)^2}{A} + \delta \tag{4.2}$$

where

$$\begin{aligned} a_v &= 15.56 \text{ MeV}, \; a_s = \; 17.23 \text{ MeV}. \\ a_c &= 0.697 \text{ MeV}, \; a_a = 23.285 \text{ MeV}. \end{aligned} \tag{4.3}$$

and $\delta = 12/\sqrt{A}$ MeV is a pairing correction. The magic numbers are associated with maxima in D.

Extending this idea, Buck et al. [16, 17] combined the stability indicators of the core and cluster into the quantity

$$D = \{B_A(Z_1, A_1) - B_L(Z_1, A_1)\} + \{B_A(Z_2, A_2) - B_L(Z_2, A_2)\}\,. \tag{4.4}$$

A maximum of this expression then gives the combination of core and cluster that is most stable, and hence the most likely core-cluster configuration.

The BMHP technique follows this pattern to find the optimum binary partition of a nucleus, with mass A and charge Z. For an arbitary mean value of the cluster mass $\langle A_2 \rangle$ the corresponding mean cluster charge and neutron number $\langle Z_2 \rangle$ and $\langle N_2 \rangle$ can be calculated using the no-dipole condition from Eq. (2.22). These mean values are considered to arise from a mixture of four even-even clusters

$$\begin{aligned} Z_2 - 2 \leq \langle Z_2 \rangle &\leq Z_2 \\ N_2 - 2 \leq \langle N_2 \rangle &\leq N_2. \end{aligned}$$

Their respective weights in the cluster mixture are

$$\begin{aligned} p(Z_2) &= \frac{1}{2}\left[\langle Z_2 \rangle - (Z_2 - 2)\right], \\ p(Z_2 - 2) &= \frac{1}{2}\left[Z_2 - \langle Z_2 \rangle\right], \\ p(N_2) &= \frac{1}{2}\left[\langle N_2 \rangle - (N_2 - 2)\right], \\ p(N_2 - 2) &= \frac{1}{2}\left[N_2 - \langle N_2 \rangle\right]. \end{aligned}$$

Thus the appropriately weighted $\langle D(\langle Z_2 \rangle, \langle A_2 \rangle)\rangle$, corresponding to the chosen $\langle Z_2 \rangle$ can then be determined using

$$\langle D(\langle Z_2 \rangle, \langle A_2 \rangle)\rangle = \sum_{Z_2, N_2} p(Z_2)p(N_2)D(Z_2.\, Z_2 + N_2). \tag{4.5}$$

Maxima are extracted by plotting D over a range of average $\langle Z_2 \rangle$ values, as seen in Figure 4.1 for ^{228}Th. The data have been smoothed using a Fourier filter [17]. The first maximum at $\langle Z_2 \rangle = 8.5$ is the exotic cluster, and the other main peak has been linked with superdeformation [25, 43].

4.3 Core-cluster decompositions

Buck et al. [17] obtained D-plots for most of the even isotopes of Radium, Thorium and Uranium, and hence deduced values of $\langle Z_2 \rangle$ corresponding to exotic clustering. Values for nine more nuclei have been obtained by Buck [44], all of which are listed in Table 4.1. The results correlate very well with the exotic decay data from Table 3.1.

Nucleus	$\langle Z_2 \rangle$	Nucleus	$\langle Z_2 \rangle$
^{220}Rn	4.6 *	^{230}U	9.4
^{222}Rn	5.9 *	^{232}U	10.0
		^{234}U	10.6
^{218}Ra	3.2	^{236}U	11.3
^{222}Ra	5.8	^{238}U	12.1
^{224}Ra	6.8		
^{226}Ra	7.8	^{238}Pu	12.2 *
^{228}Ra	8.6	^{240}Pu	13.0 *
		^{242}Pu	14.0 *
^{222}Th	5.0	^{244}Pu	15.7 *
^{224}Th	6.8		
^{226}Th	7.7	^{244}Cm	14.8 *
^{228}Th	8.5	^{246}Cm	16.1 *
^{230}Th	9.2	^{248}Cm	17.3 *
^{232}Th	9.8		
^{234}Th	10.5		

Table 4.1: *The average cluster charges obtained from the BMHP technique for nuclei in the actinide region [17]. (The data marked with an asterix are unpublished [44].)*

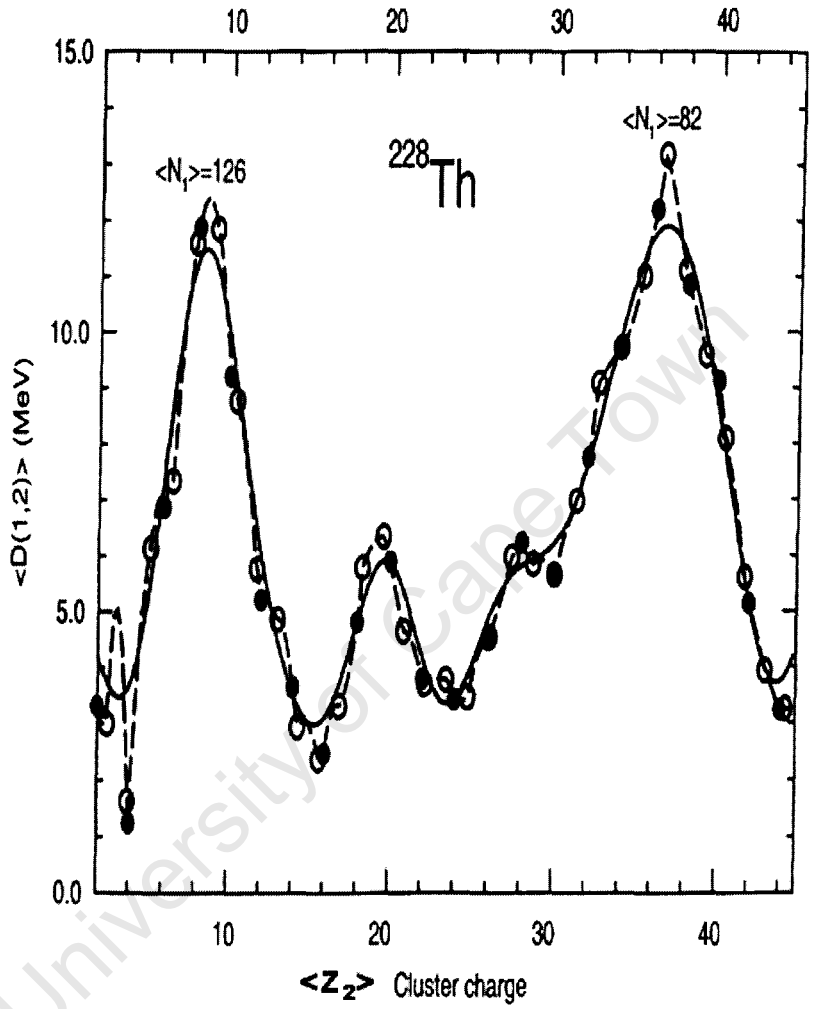

Figure 4.1: *A typical example of the resulting D-plot from the BMHP technique applied to* ^{228}Th *[17], clearly showing a peak at* $\langle Z_2 \rangle = 8.5$ *which is in good agreement with the observed decay of* $^{228}Th \rightarrow {}^{208}Pb + {}^{20}O$*, where* $Z_2 = 8$*. The second peak at* $\langle Z_2 \rangle = 36.5$ *can be related to superdeformation [25, 43]. The dashed and solid lines correspond to the 'raw' and Fourier smoothed D-plots [17].*

Chapter 5

Spectra

Nuclei can be excited into higher energy states through nuclear reactions whereby energy is transferred from an incident particle to a target nucleus. The nucleus' spectrum can then be determined from the energies of the γ-rays emitted as it decays to lower energy states [42]. As discrete spectra are a fundamental characteristic of a bound quantum system, they provide an excellent check on theory, and Buck et al. have used spectra as an important check on their various cluster model calculations. Until recently however they had not utilized the spectra as a means to extract directly the core-cluster decompositions from experimental data and thus to provide a comparison for the decompositions obtained from other methods. This has now been done successfully throughout the rare-Earth region [24], and we apply here the method to the actinide region.

5.1 Bohr-Sommerfeld relation

For a stationary state the Bohr-Sommerfeld quantization rule "fixes the energy levels of the discrete spectrum" [45] such that*

$$\int_{r_1}^{r_2} \mathrm{d}r \sqrt{\frac{2\mu}{\hbar^2}\left[E_{nL} - V(r,R)\right]} = (2n+1)\frac{\pi}{2} \tag{5.1}$$

$$\text{or} \quad \int_{r_1}^{r_2} \mathrm{d}r \sqrt{\frac{2\mu}{\hbar^2}\left[E_{nL} - V(r,R)\right]} = (G-L+1)\frac{\pi}{2}. \tag{5.2}$$

The following discussion will explore how we used this condition to find core-cluster configurations and potential parameters that optimize the fits to experimental spectra.

5.2 The spectrum fitting procedure

Buck et al. have outlined in detail the process of extracting the core-cluster decompositions from the experimental spectra in ref. [24] and we follow their procedure here.

*See Eq. 2.4 and 2.13

The method is similar to that of section 4.2 as it employs a mixture of core-cluster combinations. An even cluster mass[†] A_2 is chosen and a mean cluster charge $\langle Z_2 \rangle$ is obtained using the no-dipole condition, Eq. (2.22). This mean cluster charge is taken to arise from a mixture of two clusters, both with mass A_2 and even charges $Z_2 - 2 \leq \langle Z_2 \rangle \leq Z_2$. Their respective weights are

$$p(Z_2 - 2) = \frac{1}{2}\left[Z_2 - \langle Z_2 \rangle\right]$$

$$p(Z_2) = \frac{1}{2}\left[\langle Z_2 \rangle - (Z_2 - 2)\right].$$

We treat cluster $(\langle Z_2 \rangle, A_2)$ as a single cluster of effective charge $\langle Z_2 \rangle$ and effective Q-value

$$\langle Q \rangle = \sum_{Z_2} p(Z_2) Q(Z_2, A_2). \tag{5.3}$$

The experimental energies are then $E_{nL}(exp) = \langle Q \rangle + E^*_L(exp)$ where $E^*_L(exp)$ are the observed excitation energies for the $J^\pi = L^\pi = 0^+, 2^+, \ldots, 10^+$ states of the band of interest [46, 47]. In common with Buck et al. [24] we choose $J^\pi = L^\pi = 10^+$ as the cutoff in angular momentum. As we want to treat all the nuclei consistently this choice is a trade off between including as many states in the ground state band as possible and avoiding the difficulties (e.g. band crossing) encountered at higher excitation energies. We use the symmetric core-cluster interaction of section 2.2. The potential parameter values were initially fixed at their previous values as obtained in section 3.3,

$$U_0 = 52.9\,\text{MeV};\ a = 0.73\,\text{fm};\ x = 0.33. \tag{5.4}$$

The global quantum number G was taken to be the nearest even integer to

$$G = 0.88\mu\,(A)^{1/3} \tag{5.5}$$

from Eq. (2.16) so that the treatment is completely symmetric. These are the parameters that gave good fits to the decay data (S=178) in Table 3.1. We have thus specified all the potential parameters, save the radius R. An optimum value of this parameter is generated in the following way [24]. We first choose an initial value of R so the core-cluster interaction is completely known. Then for each L we perform the integral on the left hand side of Eq. (5.2) using the values of $E_{nL} = E_{nL}(exp)$ defined above, and obtain a quantity P_{RL}, an estimate of the right hand side of Eq. (5.2). The right hand side of Eq. (5.2) can also be obtained by directly inserting G, yielding the value P_{GL}. Minimising

$$\sigma = \sum_L \left(P_{RL} - P_{GL}\right)^2 \tag{5.6}$$

gives the optimal value of R. The cluster mass is systematically increased by 2 through the range $A_2 = 6(2)34$ and the lowest overall σ then indicates the optimum cluster mass

[†]In section 4.2 arbitary values of $\langle A_2 \rangle$ were used. However since the calculations described in this chapter are quite lengthy we only consider even integer values of A_2 here.

A_2 and corresponding potential radius R. We note that the Mass Tables limit this technique to $A_2 \geq 6$ [24]. Finally we reverse the process, using the optimum values of A_2 and radius R to generate the energies $E_{nL}(theor)$ from Eq. (5.2).

We next note that the asymptotic[‡] form of the nuclear potential of Eq. (2.10) (which has the greatest effect on the decay constants, λ) is only weakly dependent on the mixing parameter x. So the value of this parameter is not uniquely determined by our previous fits to the decay data. We thus repeated the decay calculations of Chapter 3, and the spectrum fitting procedure above, using a range of x-values. We found that we could sustain the quality of the fits to the decay data while simultaneously improving the agreement between the core-cluster decompositions obtained here by fitting the spectra and the decompositions from the other methods in Chapters 3 and 4. Our final set of modified parameters were thus

$$U_0 = 55.5 \text{ MeV } a = 0.73 \text{ fm } x = 0.24, \tag{5.7}$$

with G again given by Eq. (5.5). The resulting decay constants λ are listed in Table 5.1 and show a slightly improved fit to the data (S=172) from that obtained in Table 3.1. We also fitted the spectra with the potential parameters of Eq. (5.7) and find that the resulting core-cluster decompositions (see Table 5.2) are in good agreement with the decompositions from the other methods, as summarized in Table 6.1.

In the range $A_2 = 6(2)34$ there is usually a clear minimum corresponding to the best-fit cluster mass A_2. In a few cases there appears a competing minimum at small A_2 with anomalously large values of the potential radius R. In the rare-Earth region Buck et al. [24] found that these could be eliminated by increasing the potential depth by a small percentage for small mass clusters. We follow this procedure here (increasing the potential depth of Eq. (5.7) by 10% for $A_2 = 6$ and 5% for $A_2 = 8$). More details are given in Appendix A.

[‡] $r \gg R$

Decay	Symmetric potential		λ(exp) [s^{-1}]
	R [fm]	λ(theory) [s^{-1}]	
^{222}Ra $\rightarrow^{208}$ Pb $+^{14}$ C	6.8162	9.55×10^{-12}	$(4.18 \pm 0.55) \times 10^{-12}$
^{224}Ra $\rightarrow^{210}$ Pb $+^{14}$ C	6.8445	1.50×10^{-16}	$(1.45 \pm 0.22) \times 10^{-16}$
^{226}Ra $\rightarrow^{212}$ Pb $+^{14}$ C	6.8703	1.22×10^{-21}	$(3.99 \pm 1.38) \times 10^{-22}$
^{228}Th $\rightarrow^{208}$ Pb $+^{20}$ O	6.7684	2.50×10^{-22}	$(1.32 \pm 0.26) \times 10^{-21}$
^{230}Th $\rightarrow^{206}$ Hg $+^{24}$ Ne	6.7909	2.38×10^{-25}	$(1.70 \pm 0.30) \times 10^{-25}$
^{230}U $\rightarrow^{208}$ Pb $+^{22}$ Ne	6.9175	1.37×10^{-20}	$(1.82 \pm 1.02) \times 10^{-20}$
^{232}U $\rightarrow^{208}$ Pb $+^{24}$ Ne	6.7855	2.28×10^{-21}	$(2.64 \pm 0.28) \times 10^{-21}$
^{234}U $\rightarrow^{210}$ Pb $+^{24}$ Ne	6.8067	1.19×10^{-26}	$(8.33 \pm 6.07) \times 10^{-27}$
^{234}U $\rightarrow^{208}$ Pb $+^{26}$ Ne	6.7910	8.13×10^{-27}	$(8.33 \pm 6.07) \times 10^{-27}$
^{234}U $\rightarrow^{206}$ Hg $+^{28}$ Mg	6.8352	5.46×10^{-26}	$(5.02 \pm 0.91) \times 10^{-26}$
^{236}Pu $\rightarrow^{208}$ Pb $+^{28}$ Mg	6.8278	7.62×10^{-22}	$(2.09 \pm 0.54) \times 10^{-22}$
^{238}Pu $\rightarrow^{210}$ Pb $+^{28}$ Mg	6.8466	8.50×10^{-27}	$(1.38 \pm 0.97) \times 10^{-26}$
^{238}Pu $\rightarrow^{208}$ Pb $+^{30}$ Mg	6.7672	6.91×10^{-27}	$(1.38 \pm 0.97) \times 10^{-26}$
^{238}Pu $\rightarrow^{206}$ Hg $+^{32}$ Si	6.8887	3.76×10^{-26}	$(3.72 \pm 1.35) \times 10^{-26}$
^{242}Cm $\rightarrow^{208}$ Pb $+^{34}$ Si	6.8259	1.46×10^{-24}	$(4.95 \pm 1.42) \times 10^{-24}$

Table 5.1: *Decay constants calculated using the symmetric potential with potential parameters from Eq. (5.7) and with G from Eq. (5.5). The resulting goodness of fit parameter is S=172.*

5.3 Comparison of experimental and theoretical spectra.

Table 5.2 contains the core-cluster decompositions and the values of the potential radius R obtained from the fits to the spectra. A typical selection of these fits are shown in Figures 5.1 - 5.5, where good agreement with experiment is evident, in particular the characteristic compression of the spectra as we approach mid-shell.

When collective models were discussed in Chapter 1 we noted that cluster model spectra close to a closed shell had roughly equi-spaced levels, whereas the spectra in mid-shell were more rotational-like. Rotational excitation energies E^*_J are given by

$$E^*_J = J(J+1)\Delta E \tag{5.8}$$

where $\Delta E = \hbar^2/2I$ is constant. The first excited state of ^{222}Ra in Figure 5.1 $J = 2^+$ occurs at $E^*_J = 0.11$ MeV so that $\Delta E = 1.83 \times 10^{-2}$ MeV. For a rotational nucleus the 10^+ level should then be at 2.02 MeV, in poor agreement with the experimental value of 1.17 MeV actually found. In ^{242}Cm, the first excited state $J = 2^+$ is at $E^*_J = 0.04$ MeV so $\Delta E = 6.67 \times 10^{-3}$ MeV and the prediction from the rotational model is $E_{10^+} = 0.733$ MeV, in good agreement with experiment. The cluster model correctly predicts the spectral behaviour in both cases, and spectra are reproduced successfully over the whole range of actinides.

Nucleus	A_2	$\langle Z_2 \rangle$	R [fm]
^{220}Rn	10*	3.91	6.8289
^{222}Rn	12*	4.65	6.8420
^{218}Ra	8*	3.23	6.7857
^{222}Ra	16	6.34	6.8693
^{224}Ra	18	7.07	6.7768
^{226}Ra	24	9.35	6.6636
^{228}Ra	22	8.49	6.6930
^{222}Th	12*	4.86	6.9367
^{224}Th	16	6.43	6.8982
^{226}Th	20	7.96	6.7902
^{228}Th	24	9.47	6.7839
^{230}Th	26	10.17	6.7322
^{232}Th	28	10.86	6.7951
^{234}Th	28	10.77	6.7763
^{230}U	26	10.40	6.7702
^{232}U	28	11.10	6.8232
^{234}U	32	12.58	6.7763
^{236}U	30	11.69	6.7700
^{238}U	30	11.60	6.7330
^{236}Pu	30	11.95	6.7864
^{238}Pu	30	11.85	6.7723
^{240}Pu	30	11.75	6.8574
^{242}Pu	26	10.10	6.9400
^{244}Pu	26	10.02	6.9425
^{242}Cm	30	11.90	6.8841
^{244}Cm	32	12.59	6.8626
^{246}Cm	30	11.71	6.9710

Table 5.2: *The core cluster decompositions deduced from the spectra calculations using the symmetric nuclear potential with parameters from Eq. (5.7) and G from Eq. (5.5). The asterix indicates those A_2 values that were affected by the increase in U_0, see text and Appendix A for details.*

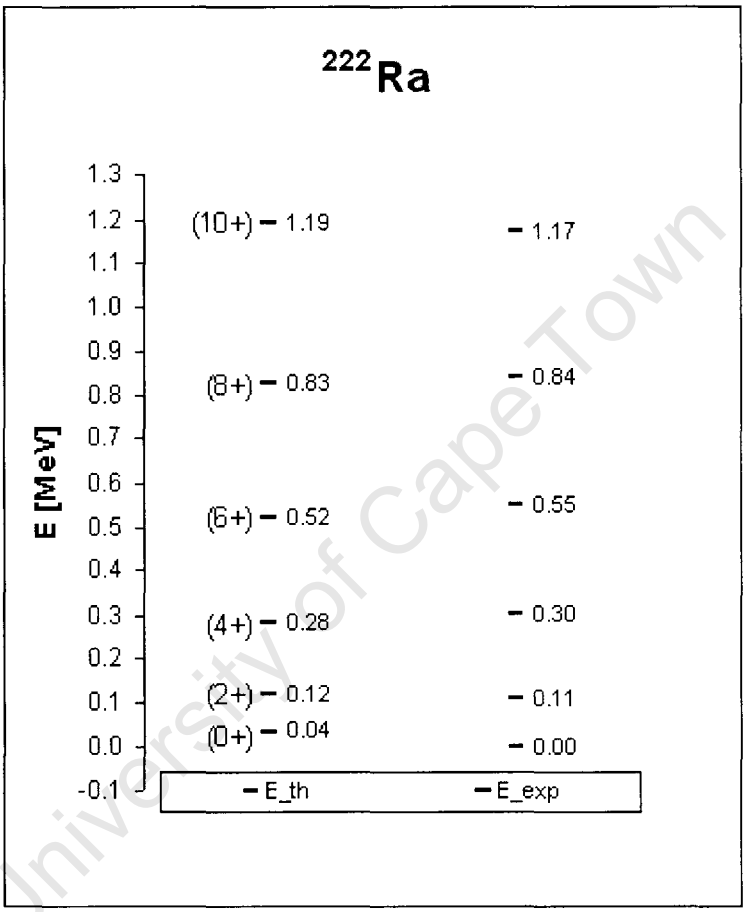

Figure 5.1: *Spectrum of ^{222}Ra generated by the cluster model (Potential parameters from Eq. (5.7), G from Eq. (5.5), and R=6.8693 fm) compared to experimental values.*

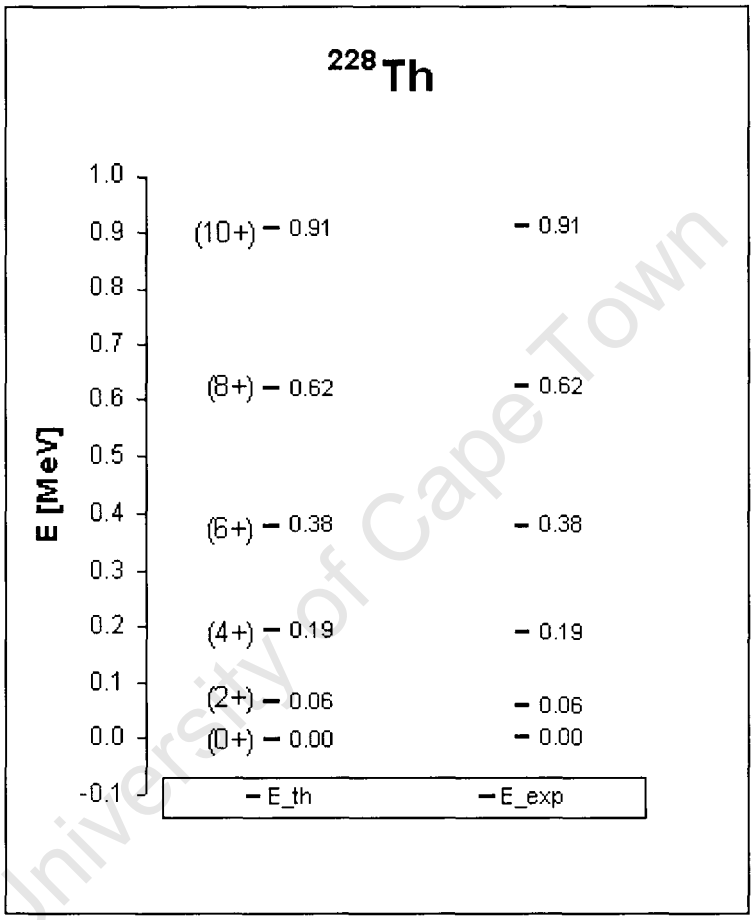

Figure 5.2: *Spectrum of* ^{228}*Th generated by the cluster model (Potential parameters from Eq. (5.7), G from Eq. (5.5), and R=6.7839 fm) compared to experimental values.*

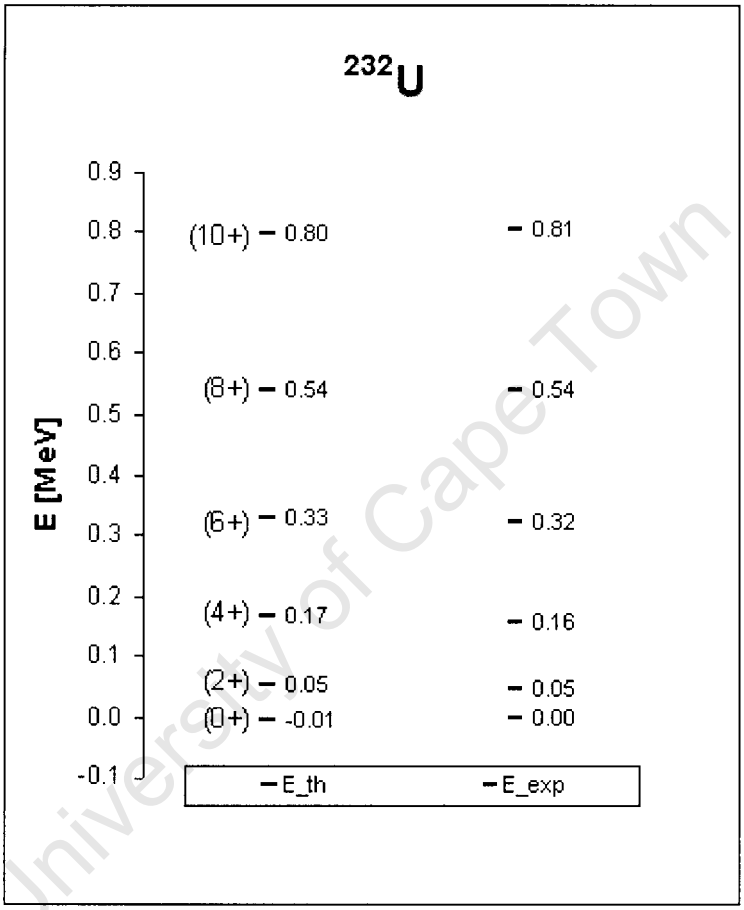

Figure 5.3: *Spectrum of ^{232}U generated by the cluster model (Potential parameters from Eq. (5.7), G from Eq. (5.5), and R=6.8232 fm) compared to experimental values.*

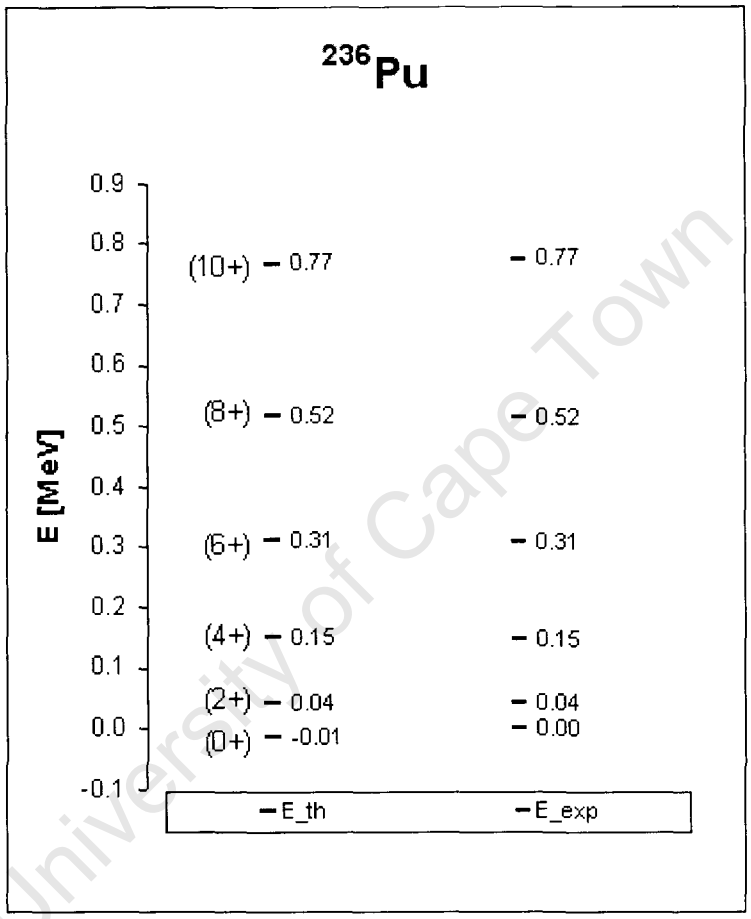

Figure 5.4: *Spectrum of* ^{236}Pu *generated by the cluster model (Potential parameters from Eq. (5.7), G from Eq. (5.5), and R=6.7864 fm) compared to experimental values.*

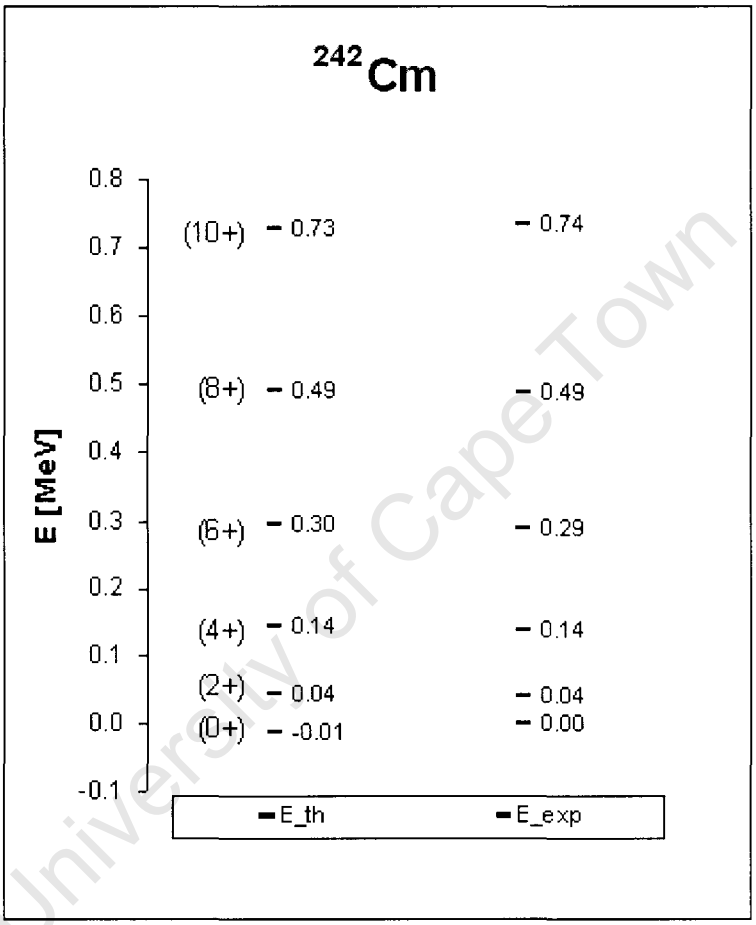

Figure 5.5: *Spectrum of* ^{242}Cm *generated by the cluster model (Potential parameters from Eq. (5.7), G from Eq. (5.5), and R=6.8841 fm) compared to experimental values.*

Chapter 6

Core-Cluster decompositions

In the preceding chapters we have implemented three methods for determining the optimal core-cluster decompositions for a given nucleus. The results obtained are now compared, and tested against the corresponding quadrupole transition strengths.

6.1 Consolidation of all the methods

The clusterizations deduced from the exotic decay data, from stability criteria, and from fitting spectra (Tables 3.1, 4.1 and 5.2 respectively) are listed along with their averages in Table 6.1. The core-cluster decompositions from all methods are consistent up to about ^{242}Pu, where the scatter exceeds 2 charge units. When nearing mid-shell the doubly magic ^{208}Pb core is perhaps unrealistically favoured in the D-plot calculations.

6.2 Testing average cluster charges against the quadrupole transition strengths

Eq. (2.26) relates B(E2) values and the charge products Z_1Z_2/Z_T. McBride utilised this aspect of the cluster model as an alternative method of determining the core-cluster decompositions in the Yb region [48] where the other methods proved less successful. Here we use the B(E2) values as an independent check on our decompositions from Table 6.1. According to the cluster model Eq. (2.26) showed that

$$\mathrm{B(E2)} \approx \frac{1}{4\pi}\left|\frac{Z_1Z_2}{Z}r_0^2A^{2/3}\right|^2. \tag{6.1}$$

Thus taking the average cluster charge from Table 6.1 and plotting $\left|\frac{(Z-<Z_2>)<Z_2>}{Z}\right|^2$ against $\mathrm{B(E2)}/A^{4/3}$ we should obtain a straight line with slope simply related to the nuclear radius parameter r_0.

In Table 6.2 we select those nuclei from Table 6.1 with an average cluster charge $\langle Z_2\rangle$ extracted from all three methods implemented here. This eliminates as far as possible

Isotope	$< Z_2 >$				B(E2) $[e^2\text{fm}^4]$
	Decay	*D-plots*	*Spectra*	*Average*	
^{220}Rn	-	4.6	3.91	4.26	3720 ± 140
^{222}Rn	-	5.9	3.10	4.50	4720 ± 300
^{218}Ra	-	3.2	2.42	2.81	2120 ± 380
^{222}Ra	6	5.8	6.34	6.05	9040 ± 760
^{224}Ra	6	6.8	7.07	6.62	7980 ± 320
^{226}Ra	6	7.8	9.35	7.72	10260 ± 560
^{228}Ra	-	8.6	8.49	8.55	12020 ± 980
^{222}Th	-	5.0	2.43	3.72	5960 ± 500
^{224}Th	-	6.8	6.43	6.62	–
^{226}Th	-	7.7	7.96	7.83	13700 ± 800
^{228}Th	8	8.5	9.47	8.66	14140 ± 540
^{230}Th	10	9.2	10.17	9.79	16080 ± 200
^{232}Th	-	9.8	10.86	10.33	18560 ± 180
^{234}Th	-	10.5	10.77	10.64	15800 ± 1400
^{230}U	10	9.4	10.40	9.93	19000 ± 2200
^{232}U	10	10.0	11.10	10.37	19800 ± 1600
^{234}U	10.67	10.6	12.58	11.28	21320 ± 400
^{236}U	-	11.3	11.69	11.50	23220 ± 300
^{238}U	-	12.1	11.60	11.85	24180 ± 400
^{236}Pu	-	-	11.95	11.95	–
^{238}Pu	12.67	12.2	11.85	12.24	25220 ± 340
^{240}Pu	-	13.0	11.75	12.38	26040 ± 600
^{242}Pu	-	14.0	10.10	12.05	26800 ± 320
^{244}Pu	-	15.7	10.02	12.86	27360 ± 320
^{244}Cm	-	14.8	12.59 *	13.70	29340 ± 340
^{246}Cm	-	16.1	11.71 *	13.91	29880 ± 340

Table 6.1: *Cluster core decompositions obtained from analysis of i) Exotic decay data ii) D-plots and iii) Spectra, and their average values, along with the experimental B(E2) values [4]. The decays of ^{234}U and ^{238}Pu have multiple decay modes so an average cluster charge is quoted in the decay column. * The two Curium isotopes have spectra that only go up to the 8^+ level.*

any biasing introduced by any one particular method of determining cluster charge. This selection is plotted as discussed above in Figure 6.1 along with the linear regression on the data.

Buck et al.'s B(E2)-plot from the rare-Earth region "deviates somewhat from the expected linearity." [49] whereas Figure 6.1 shows a good linear fit with $r_0 = 1.15 \pm 0.08$ fm, in a clearly acceptable physical range. The doubly magic ^{208}Pb may contribute to our excellent results by often occuring as the stable core.

We have indicated that the data in Table 6.2 should result in the most reliable trend

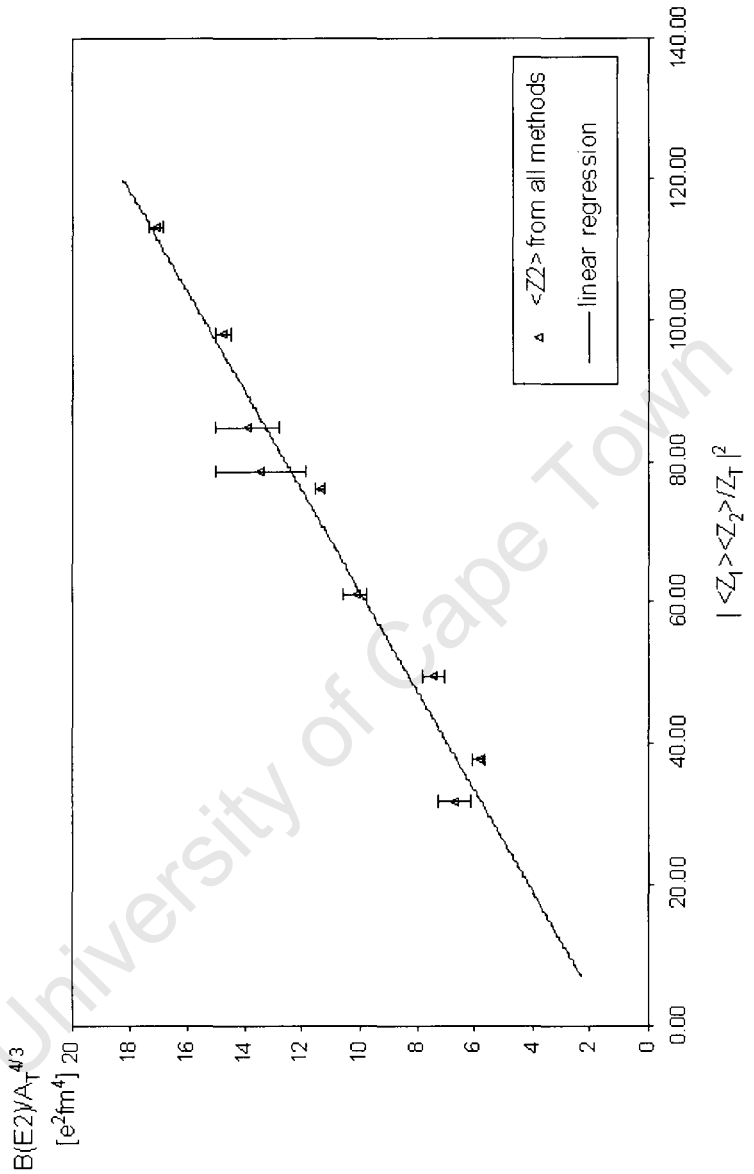

Figure 6.1: *Plot of quadrupole transitions strength against average cluster charge products using the data from Table 6.2. The solid straight line is a fit to the data.*

Isotope	$< Z_2 >$	B(E2) [e^2fm^4]
^{222}Ra	6.05	9040 ± 760
^{224}Ra	6.62	7980 ± 320
^{226}Ra	7.72	10260 ± 560
^{228}Th	8.66	14140 ± 540
^{230}Th	9.79	16080 ± 200
^{230}U	9.93	19000 ± 2200
^{232}U	10.37	19800 ± 1600
^{234}U	11.28	21320 ± 400
^{238}Pu	12.24	25220 ± 340

Table 6.2: *The average cluster charge from all three clusterization methods in Table 6.1 and the corresponding quadrupole transition strengths [4].*

line, and indeed we found that it fits all the data from Table 6.1 remarkably well, as shown in Figure 6.2. But we note that although the points in the heavier mass region in Figure 6.2 agree fairly closely with the trend line they are to be viewed with reservation as they correspond to the nuclei heavier than ^{242}Pu where Table 6.1 shows that the scatter between the decompositions from the D-plots and the spectra is large. We also note that the known spectra of the two Curium nuclei, namely ^{244}Cm and ^{246}Cm, only go up to the 8^+ level. These fits therefore cannot be considered equivalent to those fitted up to the 10^+ level. The core-cluster decomposition is especially sensitive to the input data in the heavier mass region where the clusters are larger, since large clusters produce more compressed spectra. In these cases the best fit cluster mass is not clearly distinct as $A_2 \pm 2$ give very similar spectra, thus the difference between fitting up to the 8^+ as opposed to up to the 10^+ may be significant.

6.3 Modified Casten correlations

The main purpose of any nuclear model is to understand nuclei and account for any global trends. Casten and his collaborators [50] explored certain of these trends. They found correlations between the product $N_P N_N$ of the number of valence protons (N_P) and valence neutrons (N_N) and other nuclear observables, like $E(2_1^+)$, $E(4_1^+)$ and B(E2: $2_1^+ \rightarrow 0_1^+$). Although clear correlations exist these are of a purely phenomenological nature and Casten and his collaborators [50] were unable to extract any quantitative information from them as a firm theoretical basis was lacking.

The cluster model may provide the necessary basis. Buck et al. [49] note that in the rare-Earth region Casten's plots of B(E2)/$A^{4/3}$ against $N_P N_N$ resemble the B(E2)-plots against $(Z_1 Z_2/Z)^2$ discussed in section 6.2.

The combination $(Z_1 Z_2/Z)^2$ can be related to Casten's $N_P N_N$ in the simplest case of nuclei near closed shells. In those cases the closed shell provides a likely candidate for the core and so the number of valence nucleons are just those of the cluster i.e. $N_P \sim Z_2$

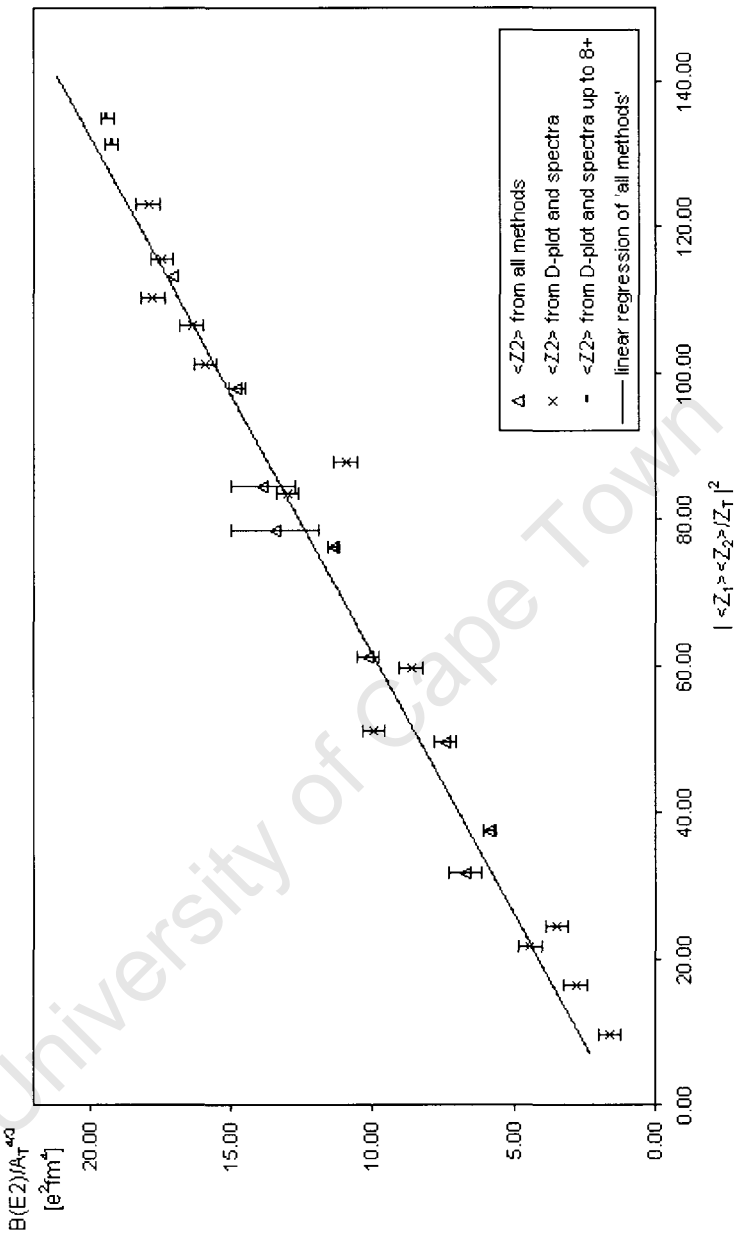

Figure 6.2: *Plot of quadrupole transition strength against average cluster charge products using the data from Table 6.1. The solid line corresponds to that in Figure 6.1. The points corresponding to Curium must be differentiated as their spectra are only known up to the* 8^+ *level.*

and $N_N \sim N_2$. For a small cluster $Z_1/Z \sim 1$ and so using the dipole rule and a binomial expansion

$$\left(\frac{Z_1 Z_2}{Z}\right)^2 \Rightarrow Z_2^2 \left(\frac{Z_1}{Z}\right)^2 \tag{6.2}$$

$$\approx Z_2 N_2 \frac{Z}{N} \left(\frac{Z_1}{Z}\right)^2 \tag{6.3}$$

$$\approx Z_2 N_2 \frac{Z}{N} \left(\frac{Z - Z_2}{Z}\right)^2 \tag{6.4}$$

$$\approx Z_2 N_2 \frac{Z}{N} \left(1 - \frac{Z_2}{Z}\right)^2 \tag{6.5}$$

$$\approx Z_2 N_2 \frac{Z}{N} \left(1 - \frac{2Z_2}{Z}\right) \tag{6.6}$$

$$\Rightarrow N_P N_N \frac{Z}{N} \left(1 - \frac{2N_P}{Z}\right) \tag{6.7}$$

where Z/N is essentially constant in any small region of the periodic table, and for the actinides $Z/N \approx 2/3$. So Casten's variables are related to the B(E2) values by the expression

$$\mathrm{B(E2)} A^{-4/3} \approx \frac{1}{4\pi} r_0^4 \frac{Z}{N} N_P N_N \left(1 - \frac{2N_P}{Z}\right). \tag{6.8}$$

Through the relationship of Eq. (6.8) we can compare the B(E2)-plots from the cluster model (Figure 6.1 and 6.2) to Casten's original $N_P N_N$ correlation (Figure 6.3) and the present adaption of it (Figure 6.4). This new Casten correlation approaches linearity in the lower mass region* and its gradient can be interpreted as

$$\frac{1}{4\pi} \left(\frac{Z}{N}\right) r_0^4 \approx \frac{1}{4\pi} \left(\frac{2}{3}\right) r_0^4. \tag{6.9}$$

The line through the origin that best fits the data in Figure 6.4 gives a value of $r_0 = 1.17 \pm 0.04$ fm, exhibiting the quantitative content of the modified Casten correlation shown.

Casten's other plots can also be interpreted in terms of the cluster model [49, 51] and will hopefully give further insight as to the model's applicability throughout the periodic table.

*The same scales were used for both Figures 6.3 and 6.4 and the improvement towards linearity in the latter is clear.

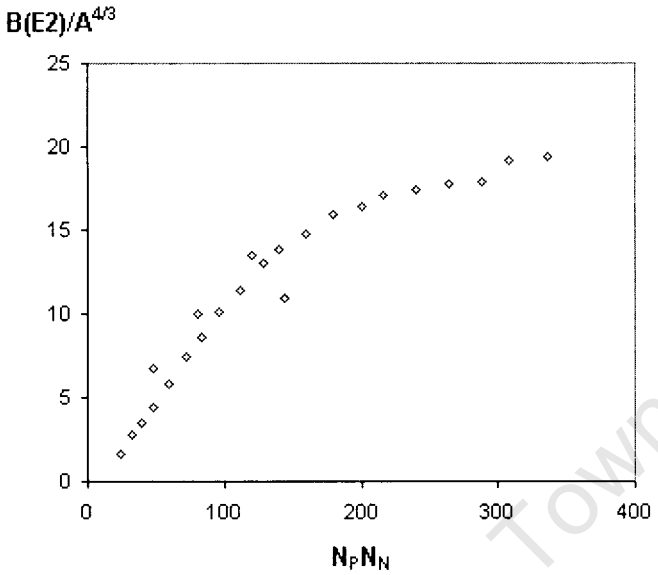

Figure 6.3: *Casten correlation of quadrupole transition stengths with* $N_P N_N$.

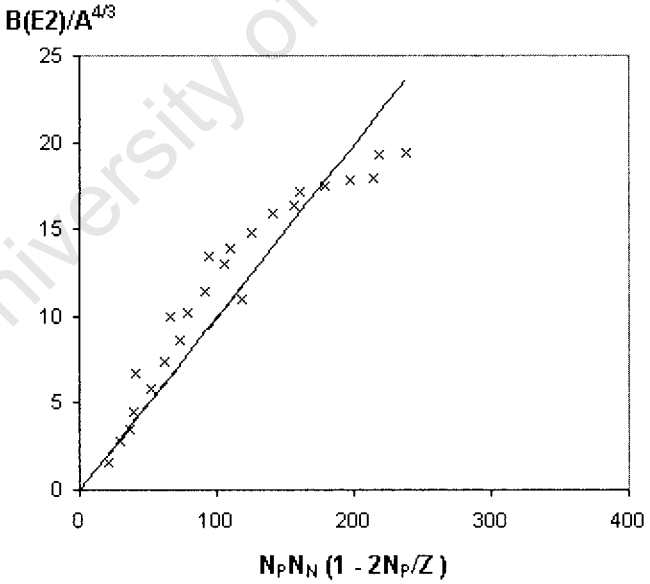

Figure 6.4: *Modified Casten correlation of transition strengths with* $N_P N_N(1 - 2N_P/Z)$.

Chapter 7

Conclusions

The heavy nucleus is a complex object with ~ 200 nucleons interacting through complicated forces; it is hard to believe that a simple two body description of the system with a straightforward potential can reproduce experimental data with some success. Yet we have shown that the binary cluster model, described in Chapter 2, can successfully reproduce a wide range of nuclear data in a consistent fashion.

Buck et al. have extended the range of applications of the binary cluster model over the last 15 years and the concept has proven robust. They were successful in their early work with alpha clusters, and subsequently with generalizations to heavier clusters. In this work we have revisited exotic decay. Using the latest decay data we extracted the core-cluster decompositions and generated theoretical disintegration constants in good agreement with experiment. We did this with both the asymmetric and the symmetric form of the core-cluster interaction. In the latter case we corrected an inconsistency in Buck et al.'s applications by showing that it is also necessary to use a mass symmetric form of the global quantum number.

A further independent way to partition the nucleus into core and cluster is the BMHP technique that uses the combination of core and cluster that maximizes the overall stability. The D-plots for the actinides show clear maxima at the preferred cluster, although possibly with some bias towards a doubly magic ^{208}Pb core.

There is also a great body of experimental data about nuclear structure in nuclear energy levels. We have utilized this by applying a new method of finding the core-cluster decompositions by fitting the experimental spectra. As a by-product theoretical spectra for nuclei with $218 \leq A \leq 246$ were generated in excellent agreement with their experimental counterparts, in particular reproducing the characteristic compression observed with increasing mass away from the closed shell. Good agreement between the three methods of partitioning is clear from Table 6.1.

The cluster model proposes a simple linear relationship between the quadrupole transition strengths and the core-cluster charge products, with the constant of proportionality related to the nuclear radius parameter r_0. We used the average cluster charges

from the decay, the D-plots and the spectra and tested this relationship. This resulted in the excellent linear correlations of Figures 6.1 and 6.2 with a value of r_0 in an expected physical range. This led us to modify Casten's correlation between B(E2)-values and $N_N N_P$ and to propose the cluster model as the theoretical basis of Casten's observations.

The cluster model is widely accepted in lighter nuclei. We have shown here that it can also be successfully applied to the actinides.

Bibliography

[1] E. N. da C. Andrade, *Rutherford and the nature of the atom* (Heinemann, London, 1965)

[2] D. B. Beard and G. B. Beard, *Quantum mechanics with applications* (Allyn and Bacon, Inc., Boston, 1970) pg 282-288

[3] C.J. Batty and G.W. Greenlees, Nucl. Phys. **A133**, 673 (1969)

[4] S. Raman, C.W. Nestor Jr, S. Kahane and K.H. Bhatt, At. Data Nucl. Data Tables **42**, 1 (1989)

[5] A. Bohr and B. R. Mottelson, *Nuclear Structure Volume 2: Nuclear Deformations* (World Scientific, London, 1975) pg 341-348, 654-656

[6] K.S. Krane *Introductory Nuclear Physics*, (John Wiley & Sons, New York, 1988) pg 139-142, 246-257, 331-333

[7] B. Buck, J.C. Johnston, A.C. Merchant and S.M. Perez, Phys. Rev. **C52**, 1840 (1995)

[8] K. Wildermuth and T. Kanellopoulos, Nucl. Phys. **7**, 150 (1958)

[9] B. Buck, A.C. Merchant, S.M. Perez and H.E. Seals, Accepted for publication in J. Phys. **G** (2005)

[10] B. Buck, A.C. Merchant and S.M. Perez, J. Phys. **G17**, 1223 (1991)

[11] F. Michel et al. Phys. Rev. **C28**, 1904 (1983)

[12] S. Ohkubo (Ed.) Prog. Theor. Phys. Suppl. **132** (1998); S. Ohkubo, Phys. Rev. Lett. **74**, 2176 (1995); M. Fukada et al. Phys. Rev. **C71**, 067602 (2005)

[13] B. Buck, A.C. Merchant and S.M. Perez, Phys. Rev. Lett. **76**, 380 (1996)

[14] K. Ikeda, Proc. Fifth Int. Conf. *Clustering Aspects in Nucl. and Subnucl. Systems*, Kyoto 1988. J. Phys. Soc. Jpn. **58**, 277 (1989)

[15] E. Uegaki Prog. Theor. Phys. Suppl. **132**, 135 (1998)

[16] B. Buck, A.C. Merchant and S.M. Perez, Few-Body Systems **29**, 53 (2000)

[17] B. Buck, A.C. Merchant, M.J. Horner and S.M. Perez, Phys. Rev. **C61**, 024314 (2000)

[18] B. Buck, A.C. Merchant and S.M. Perez, Phys. Rev. Lett. **65**, 2975 (1990)

[19] B. Buck, A.C. Merchant and S.M. Perez, Phys. Rev. **C45**, 2247 (1992)

[20] B. Buck, J.C. Johnston, A.C. Merchant and S.M. Perez, Phys. Rev. **C53**, 2841 (1996)

[21] B. Buck, A.C. Merchant and S.M. Perez, Nucl. Phys. **A614**, 129 (1997)

[22] B. Buck, A.C. Merchant and S.M. Perez, Nucl. Phys. **A652**, 211 (1999)

[23] B. Buck, A.C. Merchant and S.M. Perez, Nucl. Phys. **A657**, 267 (1999)

[24] B. Buck, A.C. Merchant and S.M. Perez, Phys. Rev. **C71**, 014311 (2005)

[25] B. Buck, A.C. Merchant, M.J. Horner and S.M. Perez, Nucl. Phys. **A673**, 157 (2000)

[26] J.M. Blatt and V.F. Weisskopf *Theoretical Nuclear Physics* (John Wiley & Sons, New York, 1952) pg 583-600

[27] B. Buck, A.C. Merchant and S.M. Perez, Nucl. Phys. **A617**, 195 (1997)

[28] B. Buck, A.C. Merchant and S.M. Perez, Phys. Rev. **C59**, 750 (1999)

[29] E. Rutherford, Nobel Lecture (1908) [online] Available: http://nobelprize.org/chemistry/laureates/1908/rutherford-lecture.html [2005, October 24]

[30] A. Sandulescu, D.N. Poenaru, W Greiner and JH Hamilton, Phys. Rev. Lett. **54**, 490 (1985)

[31] H.J. Rose and G.A. Jones, Nature **307**, 245 (1984)

[32] J. Maddox, Nature **307**, 207 (1984)

[33] S.W. Barwick, P.B. Price and J.D. Stevenson, Phys. Rev. **C31**, 1984 (1985)

[34] R.W. Gurney and E.U. Condon, Phys. Rev. **33**, 127 (1929)

[35] P.T. Matthews, *Introduction to Quantum Mechanics*, (McGraw-Hill, London, 1968) 2nd Ed. pg 36-42

[36] S.A. Gurvitz and G. Kälbermann, Phys. Rev. Lett. **59**, 262 (1987)

[37] I. Perlman and J.O. Pasmussen, Hand. Phys. XLII, 109 (1957)

[38] B. Buck, A.C. Merchant, S.M. Perez and P. Tripe, Phys. Rev. **C47**, 1307 (1993)

[39] R. Bonetti and A. Guglielmetti, *Heavy Elements and Related New Phenomena* Ed. W. Greiner and R.K. Gupta, World Scientific, Singapore (1999)

[40] A. Guglielmetti, Proceedings of *Exotic nuclei at the proton drip line* (Camerino, Italy) Ed. C.M. Petrache and L. Bianco, Unicam (2002)

[41] A. Guglielmetti, Proceedings of *Exotic clustering, CRIS 2002* (Catania, Italy) Ed. S. Costa, A. Insolia and C. Tuvè, AIP (2002)

[42] W.S.C. Williams *Nuclear and Particle Physics* (Clarendon Press, Oxford, 1992) pg 60, 108-111

[43] B. Buck, A.C. Merchant and S.M. Perez Phys. Rev. **C63**, 014312 (2000)

[44] B. Buck private communication

[45] A. Messiah *Quantum Mechanics* (North-Holland, Amsterdam, 1964) vol. 1 pg 214-241

[46] J.F.C. Cocks et al. Phys. Rev. Lett. **78**, 2920 (1997)

[47] Evaluated and Compiled Nuclear Structure Data [online] (updated: 2005, September 26) published in *Nuclear Data Sheets.* Available: http://www.nndc.bnl.gov/ensdf/ [2005, October 19]

[48] V.A. McBride, MSc Thesis, University of Cape Town, 2004

[49] B. Buck, A.C. Merchant and S.M. Perez, Phys. Rev. Lett. **94**, 202501 (2005)

[50] R.F. Casten and N.V. Zamfir, J. Phys. **G22**, 1521 (1996)

[51] B. Buck, A.C. Merchant, S.M. Perez and H.E. Seals, In preparation

Appendix A

Discussion of minima attained in the least squares fit of the spectra

We noted that when fitting the spectra as outlined in Chapter 5 that occasionally a second minimum of the goodness of fit parameter σ appears. σ is defined in Eq. (5.6) as

$$\sigma = \sum_{L} [P_{RL} - P_{GL}]^2 . \tag{A.1}$$

Figures A.1 – A.5 show some typical cases. The second minimum tends to occur when the cluster mass is small with a radius parameter larger than usual. This phenomenon also occurred in the rare-Earth region and Buck et al. found that "the systematics of R are consistent with $\sim 5\%$ increase in the value of the potential depth" [24] for small cluster mass. In the actinides we found this second minimum disappears if the potential depth of Eq. (5.7) is increased by 10% to $U_0 = 61.05$ MeV for $A_2 = 6$ and 5% for $A_2 = 8$ to $U_0 = 58.275$ MeV. Figures A.6 – A.9 show the cases in which the absolute minimum is altered by this modification of the potential depth. These four cases are listed in Table A.1, comparing the cluster properties calculated with either an unmodified or modified potential depth.

Nucleus	Unmodified potential depth		Modified potential depth	
	$\mathbf{A_2}$	**R [fm]**	$\mathbf{A_2}$	**R [fm]**
^{220}Rn	6	7.4683	10	6.8289
^{222}Rn	8	7.2306	12	6.8420
^{218}Ra	6	7.1488	8	6.7857
^{222}Th	6	7.5665	12	6.9367

Table A.1: *Comparing the best fit cluster size (and corresponding R) for the unmodified potential with $U_0 = 55.5$ MeV, and for the modified potential with ($U_0 = 61.05$ MeV for $A_2 = 6$) & ($U_0 = 58.275$ MeV for $A_2 = 8$).*

It is clear that the unmodified cases have considerably larger radius parameters R

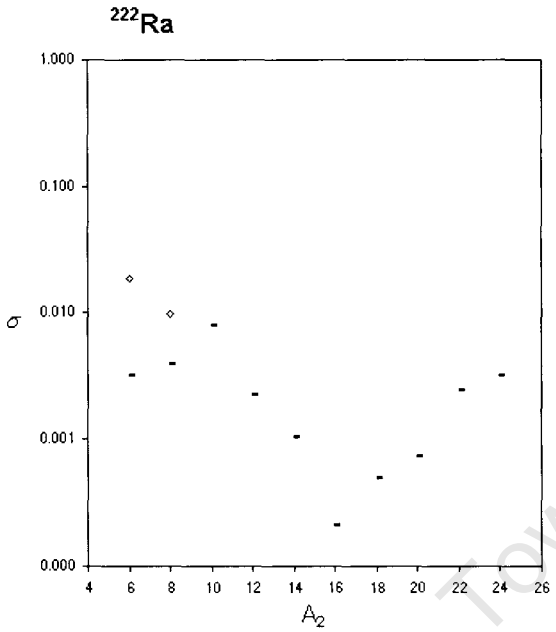

Figure A.1: *Goodness of fit parameter for ^{222}Ra: The competing minimum is clearly seen at low masses, the diamonds indicate the values of σ obtained using a modified potential depth.*

than the average of ~ 6.8 fm from Table 5.2. This anomalous behaviour is found more generally for light clusters and can be removed in all cases by the above modification to the potential depth (see Figures A.1–A.9).

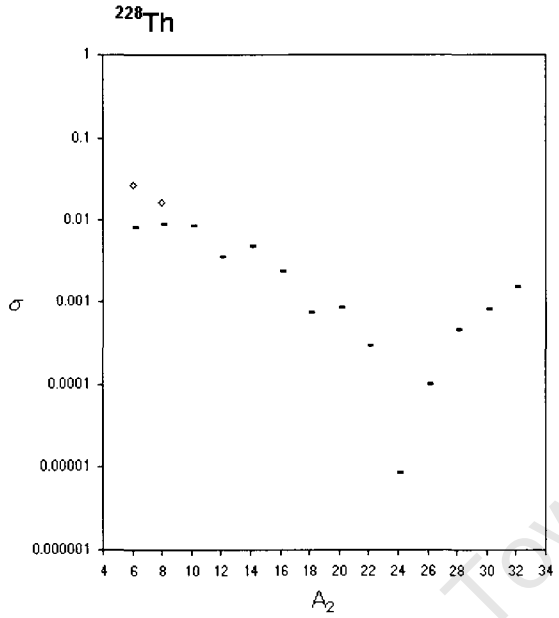

Figure A.2: *Goodness of fit parameter for* ^{228}Th*: The competing minimum is clearly seen at low masses, the diamonds indicate the values of* σ *obtained using a modified potential depth.*

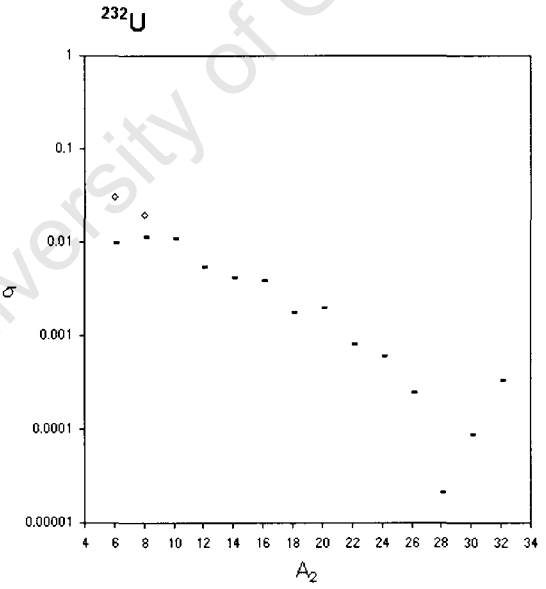

Figure A.3: *Goodness of fit parameter for* ^{232}U*: The competing minimum is clearly seen at low masses, the diamonds indicate the values of* σ *obtained using a modified potential depth.*

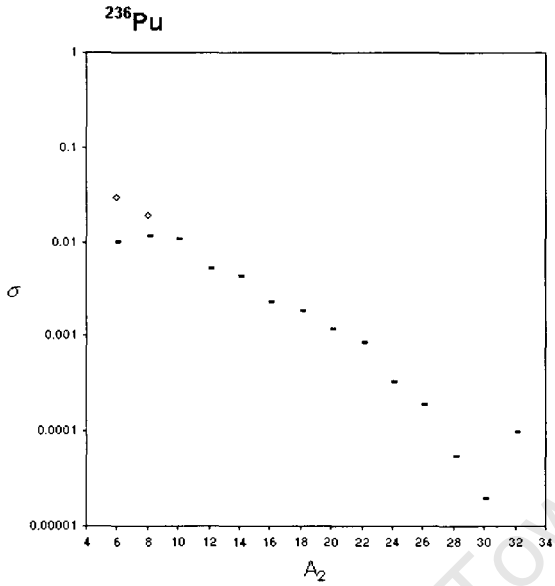

Figure A.4: *Goodness of fit parameter for ^{236}Pu: The competing minimum is clearly seen at low masses, the diamonds indicate the values of σ obtained using a modified potential depth.*

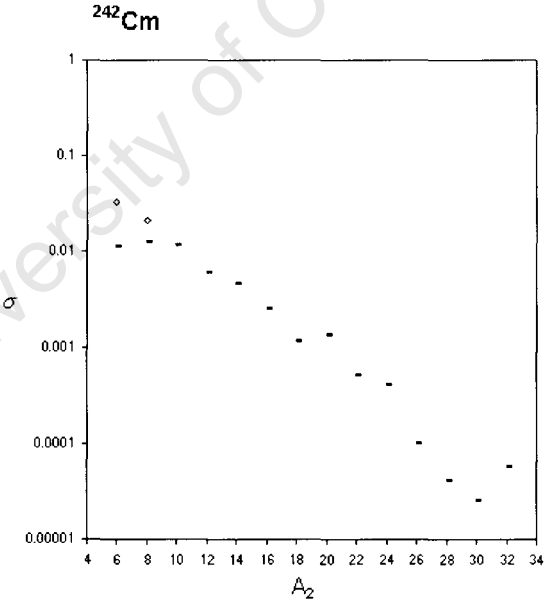

Figure A.5: *Goodness of fit parameter for ^{242}Cm: The competing minimum is clearly seen at low masses, the diamonds indicate the values of σ obtained using a modified potential depth.*

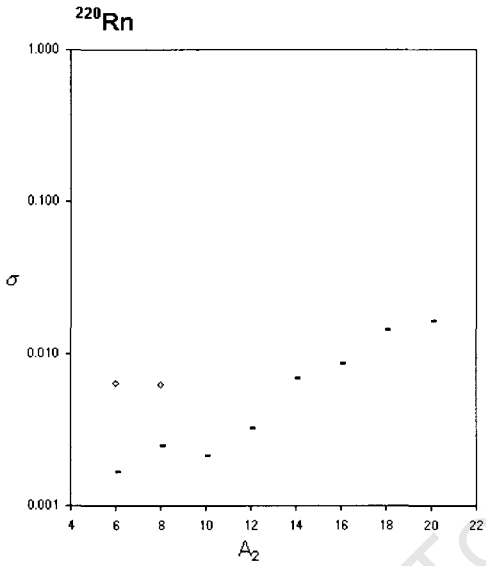

Figure A.6: *Goodness of fit parameter for* ^{220}Rn*: The competing minimum is clearly seen at* $A_2 = 6$*. The diamonds indicate the values of* σ *obtained using a modified potential depth, redefining the best fit value,* $A_2 = 10$*.*

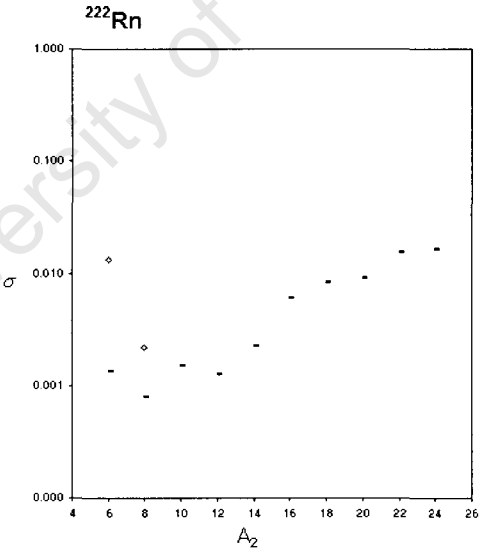

Figure A.7: *Goodness of fit parameter for* ^{222}Rn*: The competing minimum is clearly seen at* $A_2 = 8$*. The diamonds indicate the values of* σ *obtained using a modified potential depth, redefining the best fit value,* $A_2 = 12$*.*

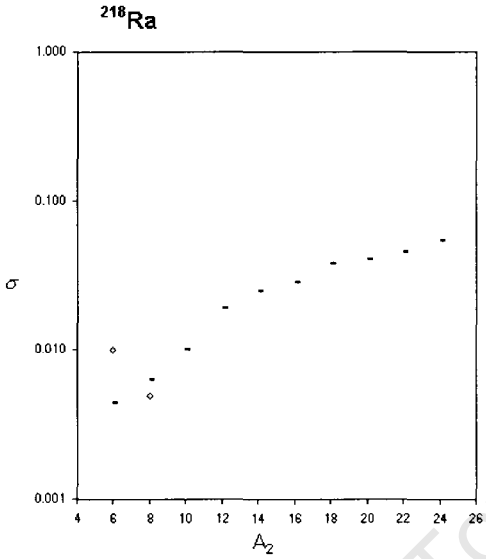

Figure A.8: *Goodness of fit parameter for* ^{218}Ra*: The competing minimum is clearly seen at* $A_2 = 6$*. The diamonds indicate the values of* σ *obtained using a modified potential depth, redefining the best fit value,* $A_2 = 8$*.*

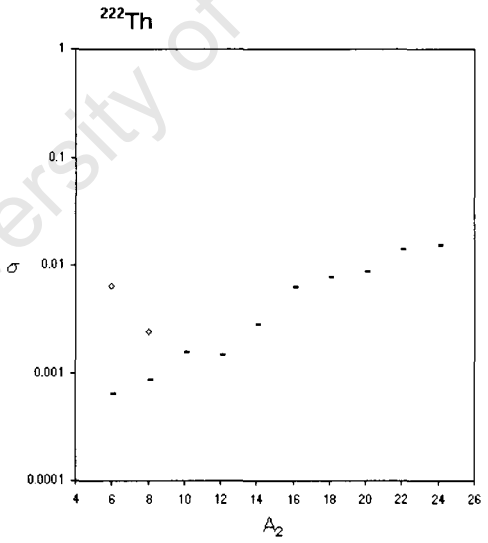

Figure A.9: *Goodness of fit parameter for* ^{222}Th*: The competing minimum is clearly seen at* $A_2 = 6$*. The diamonds indicate the values of* σ *obtained using a modified potential depth, redefining the best fit value,* $A_2 = 12$*.*

Appendix B

Description of Computer Codes

B.1 General

Two programmes were written for the calculations described in this thesis, one for obtaining the decay constants and the other for fitting the spectra. They are described in the sections below.

Both routines involve integrals whose limits are the classical turning points (r_1, r_2, r_3) of the function

$$Q + E_L^* - V(r, R) = 0, \tag{B.1}$$

see Figure 3.2. In Eq. (B.1) Q is the Q-value of the exotic decay of the nucleus (in its ground state) into the core and cluster, and E_L^* is the excitation energy of the L^{th} member of the ground state band. So given the energy of the state, $Q + E_L^*$, and the potential parameters of Eq. (5.7) the subroutine *(auto_root)* locates the positions of the classical turning points by initially stepping crudely through the specified range of $r \in \{0.0; 30.0\}$ fm and bracketing the turning points. Within the smaller interval of r defined by the bracketing the procedure is repeated with smaller and smaller steps sizes until the step size is less than 0.0001, giving the turning point to four decimal places.

All the integrals in the subsequent sections are calculated by employing the Simpson rule,

$$\int_b^a F(r)dr = \frac{h}{3}\left[F(a) + 4F(a+h) + 2F(a+2h) + 4F(a+3h) + \ldots + 4F(b-h) + f(b)\right]. \tag{B.2}$$

B.2 Decay constants

In the calculations of Chapter 3 we fit R for each nucleus to the ground state energy i.e. the Q-value. To achieve this we first use the Mass Tables to find the appropriate Q-value according to Eq. (3.1) and correct it for electron shielding using Eq. (3.10). For given potential parameters U_0, a and x, and $L = 0$ we integrate the left hand side of the

Bohr-Sommerfeld equation (Eq. (2.13)) using a starting value of R. We define

$$P_{R0} = \int_{r_1}^{r_2} \mathrm{d}r \sqrt{\frac{2\mu}{\hbar^2}\left[Q - V(r,R)\right]}. \tag{B.3}$$

The right hand side of the Bohr-Sommerfeld condition is given by $P_{G0} = \pi/2(G+1)$ and is specified by the appropriate value of G as discussed in section 3.3. We loop through a range of $R \in \{4.0; 8.0\}$ fm until $(P_{R0} - P_{G0})$ changes sign, and subsequently fine tune using increasingly smaller steps. Once we have found R to better than four decimal places, and ensured that we have a quasi-stationary state at the correct energy, the theoretical decay constant can be calculated by carrying out the integrals in Eq. (3.9).

We apply the above procedure for the fifteen nuclei that have known decay constants, for a range of $U_0 = 50(1)60$ MeV, finally fine tuning U_0 in steps of 0.1 MeV. The best U_0 corresponds to the minimum of the goodness of fit parameter S in Eq. (3.11).

B.3 Fitting Spectra

Whereas the decay calculations of Chapter 3 have an inherent core-cluster decomposition as the daughter and ejectile of the decay, the spectra calculations of Chapter 5 also involve finding the optimum decompositions. This is achieved by having an external loop involving the cluster mass and looping through a range $A_2 = 6(2)34$. Using a set of potential parameters (see section 5.2)*, a value of R for this effective cluster is obtained by a similar procedure to that outlined above in section B.2 but Eq. (B.3) becomes

$$P_{RL} = \int_{r_1}^{r_2} \mathrm{d}r \sqrt{\frac{2\mu}{\hbar^2}\left[(Q + E_L^*) - V(r,R)\right]} \tag{B.4}$$

and $P_{GL} = \pi/2(G - L + 1)$. The values of A_2 and R that produce the overall minimum of the goodness of fit parameter σ of Eq. (5.6) are taken as the optimum cluster mass and corresponding radius parameter. These optimum values are subsequently used to generate the theoretical spectra. The whole process involves multiple nested loops and is therefore very time consuming.

*Also including the small modifications of U_0 discussed in Appendix A.

Appendix C

Experimental Excitation Energies

L	^{220}Rn	^{222}Rn						
0	0.0000	0.0000						
2	0.2411	0.1864						
4	0.5338	0.4489						
6	0.8740	0.7685						
8	1.2444	1.1281						
10	1.6312	1.5130						

L	^{218}Ra	^{220}Ra	^{222}Ra	^{224}Ra	^{226}Ra	^{228}Ra	^{230}Ra	^{232}Ra
0	0.0000	0	0	0	0	0	0	0
2	0.3891	0.17847	0.11112	0.084373	0.06767	0.063823	0.0574	0.0545
4	0.7413	0.41007	0.30139	0.250786	0.21154	0.20468	0.1868	0.1792
6	1.1222	0.6881	0.55	0.4792	0.4165	0.41168	0.3791	0.3676
8	1.5468	1.0012	0.843	0.75482	0.6694	0.6741	0.6264	
10	1.9618	1.3427	1.173	1.0674	0.9599	0.9831	0.92	

L	^{220}Th	^{222}Th	^{224}Th	^{226}Th	^{228}Th	^{230}Th	^{232}Th	^{234}Th
0	0	0	0	0	0	0	0	0
2	0.3733	0.1833	0.0981	0.0722	0.057759	0.0532	0.049369	0.04955
4	0.7598	0.4398	0.2841	0.22643	0.186823	0.1741	0.16212	0.163
6	1.1658	0.75	0.5347	0.4473	0.378179	0.3566	0.3332	0.3365
8	1.5979	1.0935	0.8339	0.7219	0.6225	0.5941	0.5569	0.5648
10	2.0124	1.4611	1.1738	1.0403	0.9118	0.8797	0.827	0.843

Table C.1: *Excitation energies E_L^* in MeV [46, 47].*

L	^{230}U	^{232}U	^{234}U	^{236}U	^{238}U
0	0	0	0	0	0
2	0.05172	0.047572	0.043498	0.045242	0.044916
4	0.1695	0.15657	0.143351	0.149476	0.14838
6	0.3471	0.3226	0.296071	0.309784	0.30718
8	0.5782	0.541	0.49704	0.52224	0.5181
10	0.8564	0.8058	0.7412	0.7823	0.7759

L	^{236}Pu	^{238}Pu	^{240}Pu	^{242}Pu	^{244}Pu
0	0	0	0	0	0
2	0.04463	0.044076	0.042824	0.04454	0.0442
4	0.14745	0.145952	0.14169	0.1473	0.155
6	0.3058	0.30338	0.294319	0.3064	0.3179
8	0.5157	0.51358	0.49752	0.5181	0.535
10	0.7735	0.77348	0.7478	0.7786	0.8024

L	^{242}Cm	^{244}Cm	^{246}Cm	^{248}Cm	
0	0	0	0	0	
2	0.04213	0.042965	0.042851	0.0434	
4	0.137	0.142348	0.14201	0.1438	
6	0.288	0.296211	0.2949	0.3	
8	0.4891	0.501786	0.4998	0.508	
10	0.7359			0.765	

Table C.2: *Excitation energies E_L^* in MeV [47].*